



저작자표시-비영리-변경금지 2.0 대한민국

이용자는 아래의 조건을 따르는 경우에 한하여 자유롭게

- 이 저작물을 복제, 배포, 전송, 전시, 공연 및 방송할 수 있습니다.

다음과 같은 조건을 따라야 합니다:



저작자표시. 귀하는 원저작자를 표시하여야 합니다.



비영리. 귀하는 이 저작물을 영리 목적으로 이용할 수 없습니다.



변경금지. 귀하는 이 저작물을 개작, 변형 또는 가공할 수 없습니다.

- 귀하는, 이 저작물의 재이용이나 배포의 경우, 이 저작물에 적용된 이용허락조건을 명확하게 나타내어야 합니다.
- 저작권자로부터 별도의 허가를 받으면 이러한 조건들은 적용되지 않습니다.

저작권법에 따른 이용자의 권리는 위의 내용에 의하여 영향을 받지 않습니다.

이것은 [이용허락규약\(Legal Code\)](#)을 이해하기 쉽게 요약한 것입니다.

[Disclaimer](#)

Master's Thesis

Probing molecular interaction mechanisms of  
biopolymers

Jina Ko

Department of Chemical Engineering

Graduate School of UNIST

2020

# Probing molecular interaction mechanisms of biopolymers

Jina Ko

Department of Chemical Engineering

Graduate School of UNIST

# Probing molecular interaction mechanisms of biopolymers

A thesis/dissertation  
submitted to the Graduate School of UNIST  
in partial fulfillment of the  
requirements for the degree of  
Master of Science

Jina Ko

12/11/2019 of submission

Approved by



---

Advisor

Dong Woog Lee

# Probing molecular interaction mechanisms of biopolymers

Jina Ko

This certifies that the thesis/dissertation of Jina Ko is approved.

12/11/2019


signature



---

Advisor: Dong Woog Lee

signature



---

Jungki Ryu

signature



---

So Youn Kim

## Abstract

The discovery and identification of biomolecular interactions have improved our understanding of the unique functions of biological systems and significantly contributed to the development of nanobiotechnology. Due to the poly-functionality of biomolecules, they often employ unique combinations of individual interactions and, as a result, can form a strong ensemble of interactions with specific molecules or matter (so called *specific interaction* or *molecular recognition*). Hence, the understanding of the molecular interactions is essential to design new molecules that bind to desired molecules and materials.

There have also been several attempts to rationally design biomolecules with molecular recognition capabilities rather than relying on serendipitous findings. However, most conventional studies have relied on empirical design rules because of the lack of proper experimental analysis and understanding of these biomolecular interactions. Therefore, I investigate the biomolecular interactions and techniques. Furthermore, I report the precise measurements of various interaction forces between M13 bacteriophage (or peptide) and common functional groups.

In chapter 1, I investigate various biomolecular interactions. In addition, the principles and previous research of representative techniques used to measure molecular interactions such as atomic force microscopy (AFM), quartz crystal microbalance with dissipation monitoring (QCM-D), and surface forces apparatus (SFA) are examined.

In chapter 2, I select a specific type of genetically engineered M13 bacteriophage with CNT-binding polypeptide to investigate phage interactions. The interaction forces between the phage-coated surface and five different functionalized self-assembled monolayers (carboxylic, hydroxyl, amine, methyl, and phenyl) are directly measured using an SFA. Based on the results, the pH-dependent dispersion stability of M13 phage and single-walled carbon nanotubes (SWCNT) complexes was observed.

In chapter 3, I study the molecular interactions of the peptide sequence (DSPHTELP) that is present in the main coat protein (pVIII) of the M13 phage used in chapter 2. The interaction forces between the peptide sequence and four different functionalized self-assembled monolayers (carboxylic, methyl, amine, and phenyl) were quantified in acidic condition via SFA.

These studies provide experimental techniques for quantifying the interaction forces between biomolecules and functional groups and qualitative information on the molecular interaction mechanisms of bacteriophage and peptide. Consequently, I can suggest the direction and utilization of versatile platforms based on biomolecules.

## Contents

<b>Abstract</b> .....	<b>5</b>
<b>Contents</b> .....	<b>6</b>
<b>Lists of Figures</b> .....	<b>8</b>
<b>Lists of Tables</b> .....	<b>11</b>
<b>Chapter 1. Introduction of measuring biopolymer interactions</b> .....	<b>12</b>
1.1. Previous research of biopolymer interactions .....	12
1.2. Non-covalent interactions in biopolymers .....	12
1.2.1. Van der Waals force .....	12
1.2.2. Electrostatic interaction .....	13
1.2.3. Hydration and hydrophobic forces .....	14
1.2.4. Hydrogen bonding .....	14
1.2.5. $\pi$ -interactions .....	15
1.3. Techniques of biopolymer molecular interaction .....	15
1.3.1 Atomic Force Microscopy (AFM) .....	15
1.3.2 Quartz Crystal Microbalance with Dissipation Monitoring (QCM-D) .....	16
1.3.3 Surface Forces Apparatus (SFA) .....	18
<b>Chapter 2. Molecular interactions between M13 bacteriophage and functional groups using a Surface forces apparatus (SFA)</b> .....	<b>20</b>
2.1. Introduction .....	20
2.2. Experimental section .....	21
2.2.1. Materials .....	21
2.2.2. Preparation of SAMs with different end-functional groups .....	21
2.2.3. M13 bacteriophage cultivation .....	21
2.2.4. Bacteriophage purification .....	21
2.2.5. Preparation of monolayer M13 bacteriophage surface .....	22
2.2.6. Contact angle measurements .....	23
2.2.7. Measurement of interaction forces using a Surface forces apparatus (SFA) .....	23
2.2.8. SWCNT-DSPH phage complexation .....	24
2.3. Results and discussion .....	24
2.3.1. Experimental set-up and contact angle measurements .....	24
2.3.2. Interaction force measurements .....	29
2.3.3. Complexation and dispersion of SWCNT using DSPH phage .....	36

2.3.4 Discussion .....	38
2.4. Conclusions .....	38
<b>Chapter 3. Investigation of adhesion mechanisms in CNT-binding peptide .....</b>	<b>39</b>
3.1. Introduction .....	39
3.2. Experimental section .....	39
3.2.1. Material .....	39
3.2.2. Synthesis of peptide .....	40
3.2.3. Synthesis of triethoxysiloxane capped peptide .....	40
3.2.4. Preparation of peptide layer on mica surface .....	41
3.2.5. Preparation of end-functionalized self-assembled monolayer .....	41
3.2.6. Measurements of adhesion force using Surface forces apparatus (SFA) .....	41
3.3. Results .....	41
3.3.1. Synthesized peptide .....	41
3.3.2. Formation of a peptide layer on mica substrate .....	42
3.3.3. Adhesion energy measurements via SFA .....	44
3.4. Discussions .....	46
3.5. Conclusions .....	46
<b>Chapter 4. Summary .....</b>	<b>47</b>
<b>Chapter 5. Reference .....</b>	<b>49</b>
<b>Chapter 6. Acknowledgement .....</b>	<b>55</b>



## Lists of Figures

**Figure 1.1.** Schematic of operating process in atomic force microscopy (AFM).

**Figure 1.2.** Scheme of measuring interaction force via surface forces apparatus (SFA). **a** Interference fringes can be observed when light passes through two cross cylindrical disks in the SFA chamber and arrives at the spectrometer. **b** Force-distance curve regarding the radius of the disk. It is induced as the two cross cylindrical disks in the SFA chamber approach and retract through the double cantilevers connected to the lower disk holder.

**Figure 2.1.** AFM images of the M13 bacteriophages with CNT-binding sequences (i.e., DSPH phage) deposited on atomically flat mica surfaces. Prior to their deposition, the mica substrates were treated with a 0.1 M  $\text{MgCl}_2$  solution to replace the surface  $\text{K}^+$  ions with  $\text{Mg}^{2+}$  ions. The deposited density of the DSPH phages could be controlled by varying the concentration of the phage solution: **a**  $6.52 \times 10^9$  pfu  $\text{mL}^{-1}$  **b**  $6.52 \times 10^{10}$  pfu  $\text{mL}^{-1}$  and **c**  $2.74 \times 10^{12}$  pfu  $\text{mL}^{-1}$ . Scale bar is 1  $\mu\text{m}$ .

**Figure 2.2.** Experimental Scheme. **a** Surface forces apparatus set-up for measuring interaction forces between the functionalized SAM layer (top surface) and M13 bacteriophage deposited on mica (bottom surface). **b** Functionalized SAM layer on gold surface. **c** Molecular structure of five different alkanethiols for the formation of the functionalized SAM layers. **d** AFM image of M13 bacteriophage on mica. Scale bar, 1  $\mu\text{m}$ . **e** Structure of the M1-3 bacteriophage.

**Figure 2.3.** The wetting properties of the functionalized SAMs and DSPH. Contact angle values of **a** functionalized SAMs and **b** DSPH-coated surface as a function of pH and/or waiting time. The error bars represent the s.e.m. (standard error of mean) where  $n \geq 7$ .

**Figure 2.4.** Force vs. distance profiles measured at pH 3.0. The interactions force of the DSPH-coated surface was measured against SAMs with five different terminal functional groups: **a**  $-\text{COOH}$ , **b**  $-\text{OH}$ , **c**  $-\text{NH}_2$ , **d**  $-\text{CH}_3$ , and **e**  $-\text{Ph}$ . The empty and solid arrows correspond to the approach and detachment of the two surfaces, respectively. The orange and sky-blue curves correspond to the force-profiles at contact times ( $t_c$ ) of 5 s and 1 h, respectively. **f** Bar-graph showing the overall adhesion energy ( $W_{\text{ad}}$ ) of different SAMs at pH 3.0 as a function of contact time. The error bars represent the s.e.m. where  $n = 5$  in each group.

**Figure 2.5.** AFM images showing the influence of the terminal functional groups on the molecular interactions between the DSPH bacteriophages and the SAMs. **a** COOH-terminated and **b** CH<sub>3</sub>-terminated SAMs. The concentration of the DSPH phage solution was maintained at  $2.74 \times 10^{12}$  pfu mL<sup>-1</sup>. Scale bar is 1  $\mu$ m.

**Figure 2.6.** Force vs. distance profiles measured at pH 8.5. The interactions force of the DSPH-coated surface was measured against SAMs with five different terminal functional groups: **a** -COOH, **b** -OH, **c** -NH<sub>2</sub>, **d** -CH<sub>3</sub>, and **e** -Ph. The empty and solid arrows correspond to the approach and detachment of the two surfaces, respectively. The red and blue curves correspond to the force-profiles at contact times ( $t_c$ ) of 5 s and 1 h, respectively. **f** Bar-graph showing the overall adhesion energy ( $W_{ad}$ ) of different SAMs at pH 8.5 as a function of contact time. The error bars represent the s.e.m. where  $n = 5$  in each group.

**Figure 2.7.** Change in the thicknesses ( $\Delta D$ ) of the SAMs before and after contact with the DSPH phage-coated surface for 1 h. The observed decrease in thicknesses ( $\Delta D < 0$ ), irrespective of types of the terminal functional groups, indicated that rearrangement or reorganization of the coat-proteins in the DSPH phage occurred over time. The error bars represent the s.e.m. ( $n = 5$  in each group).

**Figure 2.8.** Force-distance profiles of Ph-SAM vs. DSPH-coated surface,  $t_c = 1$  h. **a** at pH 3.0 and **b** at pH 8.5 **c** Instantaneous detachment was observed from ① to ② at pH 3.0, while **d** gradual peel off was observed from ① to ② at pH 8.5 until ③ final detachment.

**Figure 2.9.** Dispersion stability of SWCNT-DSPH complex at different pHs. **a** Graphical illustration showing a list of potential interactions between the DSPH phages and SWCNTs upon their complexation. **b** Photographs of SWCNT-DSPH phage complexes prepared at different pHs: 3.0, 5.0, and 8.5. Schematic illustration explaining the observed difference in their dispersion stabilities. **c** The corresponding AFM images of SWCNT-DSPH phage complexes. Scale bar, 100 nm.

**Figure 3.1.** Analyzed results of the synthesized DSPHTELP peptide sequence analyze. **a** MALDI-TOF **b** HPLC for the purity of refined peptide. **c** Bio-TEM image of the DSPHTELP peptide on the TEM grid.

**Figure 3.2.** Surfaces for the SFA measurements. **a** Procedure of preparing the triethoxysilane capped DSPHTELP layer on the O<sub>2</sub> plasma treated mica. **b** AFM image the peptide layer on the mica surface.

Inner box is the pH 3.0 KNO<sub>3</sub> solution contact angle image of the peptide. **c.** AFM image of the each functionalized SAMs.

**Figure 3.3.** **a** Experimental Scheme of the SFA measurements. (a-e) Force vs. distance profiles measured at pH 3.0. The interactions force of the DSPHTELP layer was measured against functionalized SAMs: **b** -COOH, **c** -CH<sub>3</sub>, **d** -Ph. **e** -NH<sub>2</sub>. The orange and navy curves correspond to the force-profiles at contact times ( $t_c$ ) of 5 s and 1 h, respectively. **f** Bar-graph showing the overall adhesion energy ( $W_{ad}$ ) of different SAMs at pH 3.0 as a function of contact time. The error bars represent the s.e.m. where  $n = 3$  in each group.

## **Lists of Tables**

**Table 2.1.** Properties of the SAMs tested in this study.

**Table 2.2.** The  $pK_a$  values of the amino acids in the surface-exposed pVIII protein of the DSPH phage.

## Chapter 1. Introduction of measuring biopolymer interactions

### 1.1. Previous research of biopolymer interactions

Biological interactions, which occur as forces between biological molecules, are complex due to the hierarchical structure of the organism, from proteins to cells, tissues, organs, and finally the entire organism. Among them, protein interactions such as protein-protein, ligand-protein, and protein-surface are controlled by the complexity of the intermolecular forces<sup>1-3</sup>. In the most representative example, the binding of the antibody to the antigen present on the cell surface is mediated by hydrogen bonding, van der Waals, hydrophobic interaction, and so on at the binding sites<sup>4</sup>. In addition to specific interactions, non-specific interactions such as electrostatic and steric effects need to be considered to regulate the interaction of biomolecules.

The forces controlling the behavior and physicochemical origin of the biomolecules have been indirectly estimated using equilibrium binding and kinetic measurements or calculated by molecular simulation modeling<sup>5, 6</sup>. The trials can be applied to small molecules, but biomacromolecules are difficult to calculate because of their large size, high complexity, and the exponential increase in the number of the interactions between solvent molecules<sup>6</sup>.

### 1.2. Non-covalent interactions in biopolymers

#### 1.2.1. Van der Waals force

Van der Waals (VDW) force is a long-distance interaction caused by changes in the electric dipole moment of the molecules. More specifically, the VDW force is classified as Keesom (permanent-permanent dipoles) interaction, Debye (permanent induced dipoles) force, London dispersion force (fluctuating-induced dipole). The VDW force between a sphere and a flat surface follows  $F = -AR/6D^2$ , depending on the distance<sup>6</sup>. As surfaces get closer, attractive force occurs. In addition, the interaction is affected by the type of material due to the Hamaker constant ( $A$ ) that controls the magnitude of the force between materials. The constant depends on the polarity, refractive index, dielectric constant, etc. of the interacting materials. The relationship is summarized according to the Lifshitz theory<sup>7</sup>.

$$A = \frac{3}{4} kT \left( \frac{\epsilon_1 - \epsilon_2}{\epsilon_1 + \epsilon_2} \right)^2 + \frac{3I}{16\sqrt{2}} \frac{(n_1^2 - n_2^2)^2}{(n_1^2 + n_2^2)^2} \quad (1.8)$$

$\epsilon$  = Static dielectric constants,  $n$  = Refractive index,  $I$  = Ionization potential ( $\sim 2 \times 10^{-18}$  J for most materials)

If non-conductive solids or liquids interact in vacuum or air ( $\epsilon_1 = n_2 = 1$ ), the Hamaker constant is about  $5-10 \times 10^{-20}$  J. When interacting in a liquid such as water, it is smaller than  $0.5-1.5 \times 10^{-20}$  J<sup>8</sup>. In

order to more accurately calculate the VDW force between individual small molecules, the London theory should be used.

The VDW force is weak relative to ionic, hydrogen bonding, and hydrophobic interactions<sup>8</sup>. The force affects molecular and surface structures<sup>9</sup>. If two molecules or surfaces interacting with each other are flexible, rearrangement of the molecules or the surfaces occurs to further improve the overall binding energy.

When modeling interaction energies and binding mechanisms of biomolecules based on VDW force, two things should be considered<sup>8</sup>. i) The primary hydration shell (or layer) prevents two surfaces from approaching distances less than 0.5 nm. ii) Thermal movement of flexible surfaces and surface groups create thermal changes or steric hydration forces to prevent both hydrated surfaces from approaching distances less than 0.5-2.0 nm. The considerations reduce the adhesion force or binding energy of the particles, making modeling difficult.

### 1.2.2. Electrostatic interaction

Electrostatic interaction is one of the main long-distance forces (~5-10 Å) in biological interactions<sup>10</sup>. It is generated when the ionized groups with the same or opposite charges approach. The charge on a particle surface in an aqueous solution is balanced by the electric double layer and increases the ion concentration between the interacting particles compared to the bulk solution. The energy of the electric double layer interaction depends on whether the surface has a constant potential or charge at below 1.5 nm<sup>8</sup>. The mean field equations of the double layer interaction cannot be valid completely at short distance range even with constant charge and potential. The phenomenon is induced by discrete co-ion effects, finite ion size effects, counterion charge fluctuation, and counterion condensation effect based on Poisson-Boltzmann equation<sup>8, 11</sup>. Therefore, the double electric interaction between charged surfaces has attractive tendency at short range.

The VDW and electrostatic interactions are generated together in the aqueous solution. Therefore, the net interaction of the interactions is described as Derjaguin-Landau-Verwey-Overbeek (DLVO) theory<sup>8, 11</sup>. In the theory, primary minimum is energy barrier that need to separate two surfaces, and secondary minimum is that the two surfaces are repulsive at all distance or weakly attractive at some short distance<sup>8</sup>.

The ion concentration of the solution decreases at the rate of  $e^{-\kappa D}$  ( $\kappa^{-1}$ = Debye screening length)<sup>6</sup>. Hence, the electrostatic interaction is calculated by  $E(D) \approx C_{ES}e^{-\kappa D}$ ,  $C_{ES}$  is a constant. In case of the neutral molecules, the interaction depends on according to molecular orientation, and the sign changes<sup>12</sup>.

### 1.2.3. Hydration and hydrophobic forces

When liquid molecules are in contact with a surface or trapped in the space between two surfaces, the attraction/repulsion, which have periodicity equal to the diameter of the water molecule, oscillate with distance<sup>8</sup>. Then, the additional solvation forces are generated between the two surfaces. The short-range solvation force on a soft surface is smoothly repulsive, while it is smoothly attractive on hydrophobic surfaces.

$$E(D) \approx -E_0 \cos\left(\frac{2\pi D}{\sigma}\right) e^{-\frac{D}{\sigma}} \text{ per unit area (1.9)}$$

$$E_0 \approx -\rho kT\sigma \approx -kT/\sigma^2 \text{ (1.10)}$$

$\sigma$  = Diameter of liquid,  $E_0$  = Final deep primary minimum at contact of two surfaces ( $D = 0$ )

If the solute-solvent or surface-solvent binding is strong, a protective solvent shell (or layer) is formed and the primary minimum value decreases. It results in better separation of the two solvent molecules, which happens in hydrophilic groups and surfaces in aqueous solutions<sup>8</sup>. The presence of primary solvation or hydration shells around macromolecules, ionic groups, and polymeric chains in aqueous solutions reduces adhesion strength and increases the volume of solute molecules, enhancing the repulsive entropic interaction between molecules<sup>8</sup>.

On hydrophobic surfaces, the hydration force is monotonically attractive<sup>8</sup>. It is distance-dependence force, and stronger than VDW force between non-polar molecules. However, the force is a kind of enhanced VDW force caused by the peculiar dielectric and proton-hopping properties of water<sup>8</sup>. Usually, the hydrophobicity of the surface is determined by the water contact angle. Water contact angles are partially hydrophobic from 75-90°, strongly hydrophobic from 100-115°, and angles over 115° are uncommon.

### 1.2.4. Hydrogen bonding

Hydrogen bonding is a short-distance force generated by electrostatic attraction between hydrogens covalently bonded to elements with strong electronegativity (usually F, O, and N). The bonding can inhibit the inter-/inter-molecular hydrogen bonding in aqueous solution because water molecule can form hydrogen bond with solute, which is proton donors or receptor. It is stronger than dispersion forces, dipole-dipole forces, and dipole-induce dipole interactions, but weaker than ionic and covalent bonding. In addition, weak hydrogen bonding is formed by hydrogen atoms bound to sulfur, chlorine, and carbon<sup>13</sup>.

Hydrogen bonding is one of the main bonds that determine the structure in biopolymers. In particular, the secondary structure of proteins ( $\alpha$ -helix and  $\beta$ -sheet) and the structure of nucleic acids are affected by hydrogen bonding<sup>14</sup>. However, helix formation in polypeptides and proteins does not

depend completely on hydrogen bonding. The reason is that the nitrogen atom of the residue of proline is not covalently bound to hydrogen<sup>15</sup>.

### 1.2.5. $\pi$ -interactions

$\pi$ -interaction is a non-covalent interaction occurring in a molecule containing aromatic ring. Electron rich  $\pi$  aromatic and electron deficient  $\pi$  aromatic interaction with cation, anion, metal, and aromatic molecules like electrostatic interaction<sup>16</sup>. Thus,  $\pi$ -interaction include  $\pi$ - $\pi$  stacking, cation- $\pi$ , anion- $\pi$ , and metal- $\pi$  interactions. The configuration of the  $\pi$ -interaction is known to be displaced, edge-to-face, sandwich, and so on<sup>16, 17</sup>. The displaced, edge-to-face configuration is favorable interaction than sandwich configuration due to balance of quadrupole-quadrupole and London dispersion force<sup>17</sup>.

The interaction relates to most chemical and biological processes and is particularly important in supramolecular assembly and recognition<sup>16</sup>. Cation- $\pi$  interaction reported that it improves binding energy by 2-5 kcal in drug receptor and protein-protein interactions<sup>18</sup>. Hence, the cation- $\pi$  interaction provides structural stability to proteins. Anion- $\pi$  interaction has not yet been analyzed well in biological systems, but it is considered importantly in studies that inhibit enzyme activity<sup>19</sup>.  $\pi$ -interaction arises mainly between proteins containing phenylalanine, tyrosine, tryptophan, and histidine in protein interactions<sup>19</sup>. In case of nucleic acids, DNA double helix structure is stabilized by the stacking interactions between DNA bases<sup>19, 20</sup>.

## 1.3. Techniques of biopolymer molecular interaction

### 1.3.1 Atomic Force Microscopy (AFM)

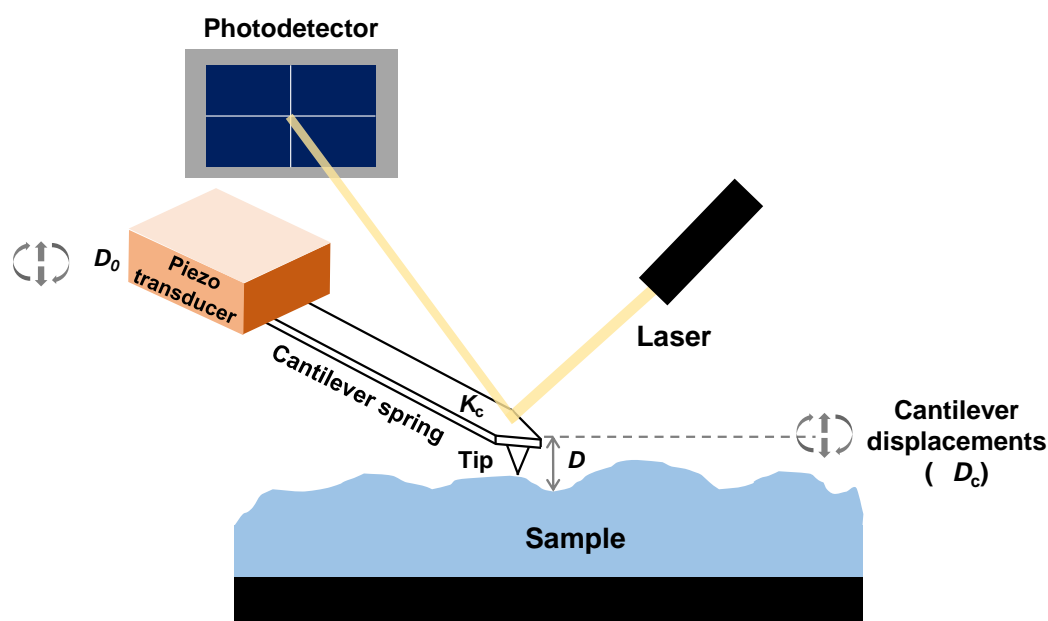


**Figure 1.1.** Schematic of the operating process in atomic force microscopy (AFM).



Atomic force microscopy (AFM) is an imaging technique which has been used to measure the interaction between biological molecules. The first result when measuring the interaction using AFM is the Biotin-avidin binding<sup>21</sup>. Since then, the interaction between protein-ligand<sup>22</sup>, protein-protein<sup>23</sup>, and protein-substrate<sup>24</sup> have been measured. In AFM, the tip (radius,  $R \sim 10-100$  nm) contacts and moves perpendicular to the surface. The molecular interaction is achieved by the rupture force obtained when the bond between the molecule on the tip and the surface breaks, resulting in a force-distance curve. To precisely measure the adhesion between molecules, a cantilever with a spring stiffness ( $K_c$ ) =  $0.01 \text{ nN}^{-1}$  is used.<sup>8</sup> The force range of the tip varies in proportion to the radius of the tip. Usually, a silicon nitride tip can measure up to  $10 \text{ pN}$ <sup>25</sup>.

$$\Delta D = \Delta D_0 - \Delta D_c \quad (1.1)$$

$$F_a = \Delta F = K_c \Delta D_c \quad (1.2)$$

$K_c$  = Spring stiffness,  $\Delta D_0$  = Substrate surface,  $\Delta D_c$  = Spring deflection,  $F_a$  = Adhesion force

Due to the small radius of the tip, the contamination problems caused by particulate rarely occur and the fluid dynamics force can be ignored during measuring the interaction force in a solution<sup>11</sup>. However, the absolute thickness of the adsorbed layer on the surface is not measured<sup>11</sup>. It is difficult to measure deformable soft materials such as biological membranes using AFM<sup>11</sup>. Furthermore, it is hard to predict which part of the molecule is stretched because the tip scans the surface until an interaction occurs between the tip and the surface<sup>8</sup>.

### 1.3.2 Quartz Crystal Microbalance with Dissipation Monitoring (QCM-D)

Quartz crystal microbalance with dissipation monitoring (QCM-D) has been utilized to study interactions at the interface because it can measure mass and viscoelasticity *in situ* with high sensitivity<sup>26-28</sup>. QCM-D is operated by placing a quartz plate between two metal electrodes and applying an alternating current (AC). As the AC frequency approaches the fundamental frequency ( $f_1$ ) of the quartz sensor, resonance occurs. When the mass of the sensor changes via molecule adsorption on the surface, the  $f_1$  and multiple harmonic frequency of the sensor also changes. QCM-D measures the interfacial interactions in such a way that the resonance frequency is continuously observed<sup>28</sup>.

Sauerbrey established an equation in which the frequency change caused by the crystal oscillation is inversely proportional to the mass adsorbed on the surface (equation 1.3)<sup>29</sup>. In addition, the thickness of the adsorption layer can be determined by the adsorption mass and density.

$$\Delta m = \frac{C}{n} \Delta f, C = \frac{t_q \rho_q}{f_0} \quad (1.3)$$

$n$  = Overtone number (in the present case  $n = 3, 5, \text{ and } 7$ ),  $t_q$  = Thickness of quartz,  $\rho_q$  = Density of

quartz (equals  $\sim 17.7 \text{ Hz} \cdot \text{ng}/\text{cm}^2$  for a 5 MHz crystal)

$$h_{eff} = \frac{\Delta m}{\rho_{eff}} \quad (1.4)$$

$\rho_{eff}$  = Effective density of adsorbed layer,  $h$  = Thickness of adsorbed layer

In order for the Sauerbrey equation to be valid, three assumptions must be satisfied<sup>28</sup>. i) The adsorbed mass should be smaller than the crystal sensor mass. ii) The adsorbed mass must be adsorbed rigidly. iii) The adsorbed mass should be evenly distributed over the active area of the crystal sensor. There are limitations to applying the equation because the frequency change is affected by viscous and elastic factors in liquid applications.

In QCM-D, the Kelvin-Voigt model is used to derive mass, thickness, density, viscosity, and storage modulus values of the adsorbed layer<sup>30</sup>. The viscoelastic data provided helps characterize the system beyond the linear Sauerbrey equation. The  $\Delta f$  and  $\Delta D$  (dissipation shift) at three different overtones of the resonant frequency can be measured in millisecond intervals. Using the overtones, the viscoelastic properties of the adsorbed layer with multiple  $\Delta f$  and  $\Delta D$  were calculated (equation 1.5-1.7)

$$G^* = G' + iG'' = \mu_1 + i2\pi f\eta_1 \quad (1.5)$$

$G^*$  = Complex shear modulus,  $G'$  = Storage modulus,  $G''$  = Loss modulus

$$\Delta f \approx -\frac{1}{2\pi\rho_0 h_0} \left\{ \frac{\eta_3}{\delta_3} + h_1 \rho_1 \omega - 2h_1 \left( \frac{h_3}{\delta_3} \right)^2 \frac{\eta_1 \omega^2}{\mu_1^2 + \omega^2 \eta_1^2} \right\} \quad (1.6)$$

$$\Delta D \approx -\frac{1}{\pi f \rho_0 h_0} \left\{ \frac{\eta_3}{\delta_3} + 2h_1 \left( \frac{h_3}{\delta_3} \right)^2 \frac{\eta_1 \omega^2}{\mu_1^2 + \omega^2 \eta_1^2} \right\} \quad (1.7)$$

$\rho_0$  = Density of crystal,  $h_0$  = Thickness of the crystal,  $\eta_3$  = Viscosity of the bulk liquid,  $\delta_3$  = Viscous penetration depth of the shear wave in the bulk liquid,  $\rho_3$  = Density of liquid,  $\omega$  = Angular frequency of the oscillation

The adsorption of proteins on biological surfaces plays an important role in biocompatibility<sup>31</sup>. Previous studies have utilized these properties of QCM-D to determine candidates to prevent unwanted protein adsorption, such as blood clotting in blood vessels<sup>32</sup>. Not only has QCM-D been used to observe the morphological changes (e.g., swelling and hydration) of adsorbed proteins<sup>33</sup>, but also measure small molecule-protein interactions and protein-polysaccharide interactions<sup>28</sup>.

While most interfacial reactions involving mass changes at the solid-liquid interface can be characterized using QCM-D, it is not possible for atoms and small molecules<sup>34</sup>. As a result, QCM-D is not suitable for studies that require the adsorption of atoms and small molecules in precise concentrations. Additionally, QCM-D cannot be used for non-smooth and non-uniform

surface/interface studies like adsorption on porous adsorbents or crystalline minerals<sup>34</sup>. Despite the drawbacks, QCM-D observes energy dissipation *in situ* and is appropriate for simulating adsorption, desorption, and dissolution under controlled fluid flows and temperatures<sup>35-37</sup>. Hence, it is good for testing the effects of surface chemistry on overall interfacial interactions and for monitoring interactions where molecular morphology or adlayer properties are important.

### 1.3.3. Surface Forces Apparatus (SFA)

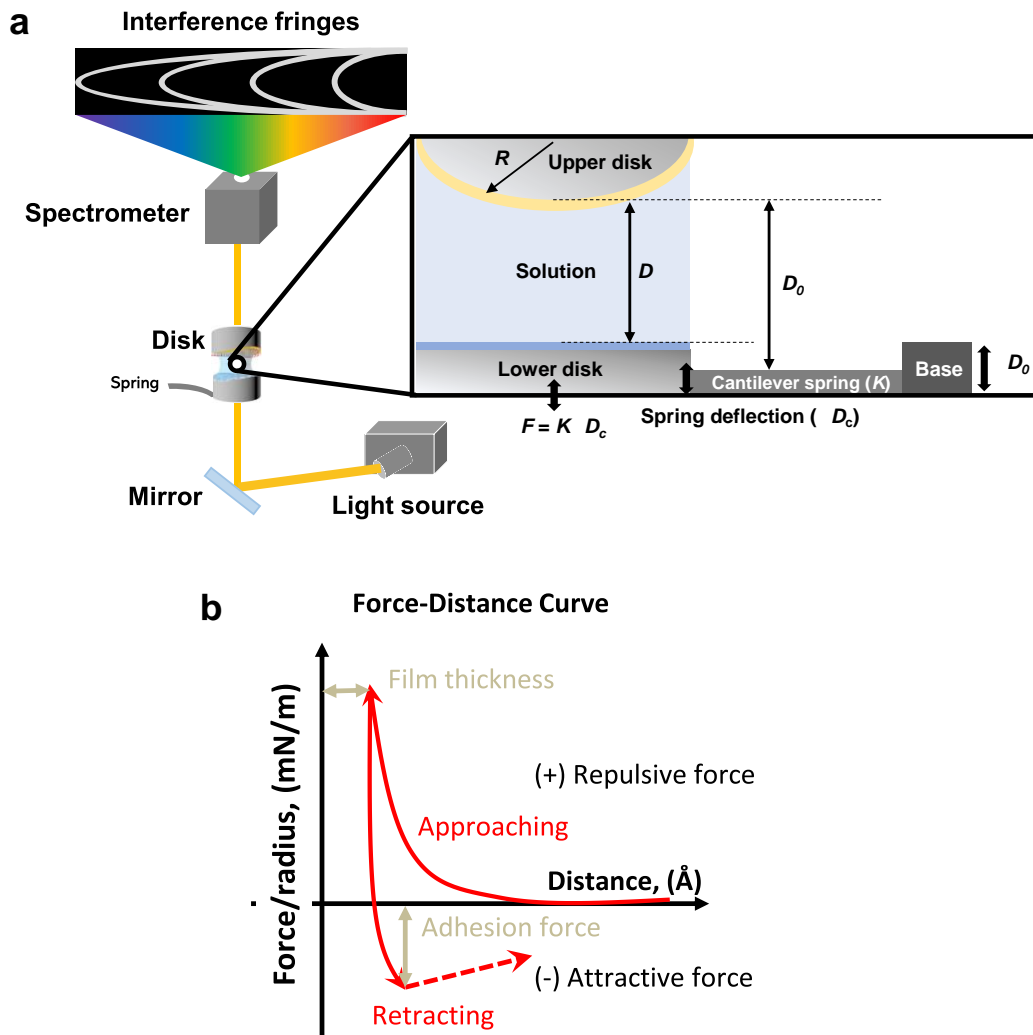


**Figure 1.2.** Scheme of measuring interaction force via surface forces apparatus (SFA). **a** Interference fringes can be observed when light passes through two cross cylindrical disks in the SFA chamber and arrives at the spectrometer. **b** Force-distance curve regarding the radius of the disk. It is induced as the two cross cylindrical disks in the SFA chamber approach and retract through the double cantilevers connected to the lower disk holder.

Surface forces apparatus (SFA) is an equipment that measures surface to surface interactions, adhesion, friction, and lubrication force, as well as van der Waals, bio-specific, steric, and hydrophobic interactions<sup>38</sup>. Hence, the SFA has been used to measure forces between surfaces with different chemical and physical properties. In particular, quantitative information on the magnitude of van der Waals, electrostatic, steric, hydration, and hydrophobic interactions between biological surfaces have been obtained.

The distance resolution of the SFA is 0.1 nm - 1  $\mu\text{m}$  and the force resolution is up to  $10^{-8}$  N<sup>11</sup>. The interactions between surfaces are measured by adjusting the distance between the two cylindrically crossed surfaces via the double-cantilever of SFA. By using the multiple beam interferometry (MBI), the thickness of the adsorbed layer and the absolute distance between the two surfaces are optically obtained from the fringe of equal chromatic order (FECO)<sup>11</sup>. More specifically, a motor connected to SFA is used to control the double cantilever that is connected to the dove tailed disk holder in the SFA chamber to make contact between the two surfaces. The FECO is monitored in real time to observe the  $\Delta D$  and surface deformation. The shape and position of the FECO change according to the shape and separation of the surfaces. In most SFA experiments, a 50 nm thick silver coated mica sheet was attached to a cylinder disk<sup>11</sup>. The silver reflects light in a direction perpendicular to the disk surface, then the focused light passes through the slit of the spectrometer and was recorded in the video camera. Therefore, a force-distance curve is obtained by considering the radius of the cylinder disk.

The adhesion force between the two surfaces is determined by measuring the distance between the contact and  $D_{\text{jump}}$  (distance after jump). A double cantilever with a different spring constant( $k$ ) should be selected depending on the adhesion of the material. According to  $F=k\Delta D$ , the higher the spring constant, the smaller the  $\Delta D$  needed to apply the required force.

SFA has the advantage that the inter-surface distance is measured by the optical interferometric technique. As the distance between two surfaces changes, the wavelength of interference fringes shifts, and surface separation is determined *in situ* with a resolution of 0.1 nm<sup>11</sup>. This resolution is not affected by surface deformation or soft material compression. The lateral resolution of SFA is not better than that of an optical microscope<sup>8</sup>. With FECO, however, the direct visualization of the contact area provides immediate detection of damage to the surface and unwanted particles or contamination. Furthermore, it is necessary to supplement SFA with other methods of surface analysis such as AFM, XPS, and ESCA to characterize the surface morphology and composition because molecular composition and structure are not analyzed by SFA<sup>11</sup>.

## Chapter 2. Molecular interactions between M13 bacteriophage and functional groups using a Surface forces apparatus (SFA)<sup>39</sup>

### 2.1 Introduction

M13 bacteriophage (or virus) is a useful biological building block for liquid crystalline structure, photovoltaic device and so on<sup>40-45</sup>. Due to its inherent nanostructure, abundant polypeptides present on its surface, and modification flexibility through genetic engineering, the M13 bacteriophage has been successfully utilized to assemble and fabricate various functional nanomaterials. Examples include hybrid materials of carbon nanotubes (CNTs) and TiO<sub>2</sub> for photovoltaics<sup>42</sup>, CNTs and inorganic materials for rechargeable batteries<sup>46</sup>, and porphyrin and IrO<sub>x</sub> for solar water splitting<sup>47</sup>.

I report the precise measurement of various interaction forces between the M13 phage and common functional groups using a surface forces apparatus (SFA) to understand the origin of its molecular recognition capability. Especially, I measure the interaction forces of the M13 phage with CNT-binding polypeptides (DSPH) along its filamentous capsid—an amino acid sequence of **DSPHTELP** on pVIII coat proteins—with various functional groups. Among various types of phages, I choose the DSPH phage for the following reasons: (1) It has a specific binding affinity towards CNTs, which can find diverse applications in various fields, such as catalysis<sup>40</sup>, biomedical engineering<sup>43</sup>, materials science<sup>42</sup>, and energy conversion and storage<sup>46</sup>. In addition, the molecular structure of CNTs are very similar to that of other carbon materials such as fullerene, graphene, and graphite. Thus, our study can provide valuable insights to a broader range of researchers. (2) Because the CNT-binding sequences of the DSPH phage were abundantly displayed (~2,700 copies) along its filamentous structure, it can provide more reliable measurement for SFA analysis than other types of phages with the CNT-binding sequences on pIII (~5 copies). In addition, a high aspect ratio and flexibility of M13 bacteriophage make it difficult to study the interaction forces for pIII proteins. (3) Practically, the DSPH phage can be more readily prepared in a large scale compared to other types of phage due to its high amplification rate in *E.coli*. Five different types of functional groups are prepared using self-assembled monolayers (SAMs) bearing different terminal groups: carboxylic (COOH), hydroxyl (OH), amine (NH<sub>2</sub>), methyl (CH<sub>3</sub>), and phenyl (Ph) groups. Direct and precise measurement of the force vs. distance curves with the SFA under various conditions allow the identification of different types of interaction forces between the M13 bacteriophages and functional groups. These provide clues to the molecular origin of its CNT-binding ability. Our results suggest that histidine and proline moieties play critical roles in the binding of the phages to CNTs and aggregate formation in aqueous solutions, respectively. These results are further confirmed by the pH-dependent behaviors of the phage complexation with the CNTs, indicating that aggregation and precipitation of the complexes can be tuned by pH. I believe that this study can provide a versatile platform to characterize various specific

biomolecular interactions and enable better understanding and utilization of biomolecules.

## **2.2 Experimental section**

### **2.2.1 Materials.**

HiPCo SWCNTs were purchased from Unidym. Unless stated otherwise, all chemicals, including 10-carboxy-1-decanethiol (95%), 11-amino-1-undecanethiol, hydrochloride (99%), 11-hydroxy-1-undecanethiol (97%), 1-undecanethiol (98%), and 2-phenylethanethiol (98%), were purchased from Sigma-Aldrich.

### **2.2.2 Preparation of SAMs with different end-functional groups.**

Each alkanethiol was prepared on atomically smooth gold surfaces. The smooth gold surfaces (thickness: 45 nm) were prepared on cleaved clean muscovite mica (Grade #1, S&J Trading, Floral Park, NY, USA) through electron beam evaporation. The gold layers were attached to the curved surfaces of cylindrical glass discs (Radius,  $R \sim 2$  cm) by painting them with an optical adhesive, Norland optical adhesive 81 (Norland Products, Inc. Cranbury, NJ, USA), and subsequently UV treating the samples for 40–60 min. The discs with gold-coated top surfaces were immersed into 1 mM alkanethiol-ethanol solution for the formation of SAM structure via gold-sulfur bonds on the gold (111) surfaces<sup>48</sup>. After 16–18 h, the discs were sonicated for 30 s, washed with ethanol, and dried by nitrogen gas to remove physical impurities and excess SAM molecules from the surfaces.

### **2.2.3 M13 bacteriophage cultivation.**

The genetically engineered M13 bacteriophage (DSPH phage) was obtained from Prof. Belcher's group at Massachusetts Institute of Technology. Cultivation of M13 bacteriophages was performed using *Escherichia coli* strain ER2738 from New England Biolab. First, 10 mL of Luria Bertani (LB) medium was mixed with 10  $\mu$ L of TET (antibiotic) and a single colony of ER2738 cells and incubated overnight. For large scale amplification, 1 mL of TET, 10 mL of the overnight culture, and about  $10^{11}$  pfu of the DSPH phage were added to a freshly prepared LB medium (25 g of LB medium and 1 g of  $\text{MgCl}_2 \cdot 6\text{H}_2\text{O}$  in 1 L of distilled water). Thus, around  $10^{14}$  pfu  $\text{mL}^{-1}$  of bacteriophages were produced. Finally, the culture was incubated in a 37 °C shaker at 225–250 rpm for about 6 h.

### **2.2.4 Bacteriophage purification.**

First, 500 mL of the culture was poured into each large centrifuge tube and centrifuged at 7,800 rpm for 30 min. After centrifugation, 70 mL of PEG/NaCl (200 g of PEG and 146 g of NaCl in 1 L deionized water) was added to a 420 mL of supernatant, and the mixture was left overnight at 4 °C. The solution was centrifuged again at 8,140 rpm for 30 min, the supernatant was discarded, and the

solution was centrifuged at 8,140 rpm for another 5 min. The white phage pellets in the centrifuged solution were dissolved completely in a 30 mL TBS solution. The solution was centrifuged at 10,000 rpm for 5 min to remove residual impurities, after which 5 mL of PEG/NaCl solution was added to the solution and mixed until the solution became homogeneous. Finally, the phage solution was centrifuged at 11,000 rpm for 30 min, the supernatant was discarded, and the solution was centrifuged again at 11,000 rpm for 5 min. The resulting phage solution concentration was determined by the amount of the white phage pellets that were obtained just before centrifuging to dissolve the 1 mL TBS solution (pH 7.2).

### 2.2.5 Preparation of monolayer M13 bacteriophage surface.

An atomically smooth mica surface was treated with a 0.1 M  $\text{MgCl}_2$  solution to replace  $\text{K}^+$  ions with  $\text{Mg}^{2+}$  ions on the surface of the mica before the deposition of the phages.<sup>49</sup> The mica substrate was subsequently treated with an M13 solution (pH 5.0) to deposit a monolayer of M13 bacteriophages through electrostatic attractions between the positively charged mica and negatively charged M13 phages. An appropriate concentration of the M13 bacteriophage solution for the preparation of a monolayer M13 phage film for SFA analysis was  $2.74 \times 10^{12}$  pfu  $\text{mL}^{-1}$  (Figure 2.1), according to morphology investigations with a Veeco multimode V\_AFM in standard tapping mode. A drop (80  $\mu\text{L}$ ) of the M13 bacteriophage solution was loaded on the  $\text{MgCl}_2$ -treated mica surface and left for 1 h. Finally, the surface was rinsed with deionized water and dried with nitrogen gas. The number density and coverage of the M13 bacteriophages on the mica substrate were analyzed using the freeware, ImageJ.

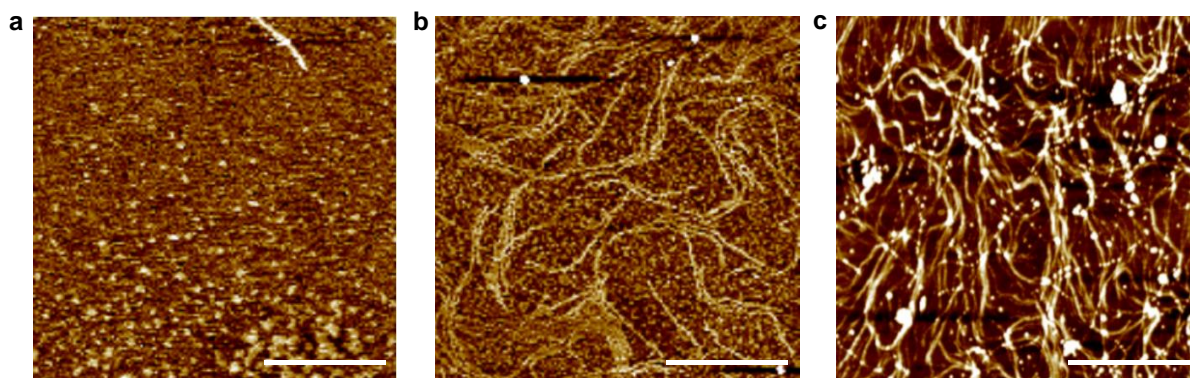


**Figure 2.1.** AFM images of the M13 bacteriophages with CNT-binding sequences (i.e., DSPH phage) deposited on atomically flat mica surfaces. Prior to their deposition, the mica substrates were treated with a 0.1 M  $\text{MgCl}_2$  solution to replace the surface  $\text{K}^+$  ions with  $\text{Mg}^{2+}$  ions. The deposited density of the DSPH phages could be controlled by varying the concentration of the phage solution: **a**  $6.52 \times 10^9$  pfu  $\text{mL}^{-1}$  **b**  $6.52 \times 10^{10}$  pfu  $\text{mL}^{-1}$  and **c**  $2.74 \times 10^{12}$  pfu  $\text{mL}^{-1}$ . Scale bar is 1  $\mu\text{m}$ .

### 2.2.6 Contact angle measurements.

Wetting properties of the M13 bacteriophages and alkanethiol compounds were investigated using a DSA-100B-basic contact angle analyzer (KRÜSS GmbH, Germany). First, 4  $\mu\text{L}$  of 3 mM  $\text{KNO}_3$  solution (pH 3.0 and pH 8.5) was dropped on each SAM surface. The contact angle values were obtained in tangent 1 fitting mode. In the case of the M13 bacteriophage-coated surface, a sample was placed in an acrylic box with wetted tissues and left for 10 min to achieve air saturation, after which a 4  $\mu\text{L}$  droplet of 3 mM  $\text{KNO}_3$  (pH 3.0 and pH 8.5) was placed on the phage surface. The measurements were recorded as a video clip for 10 min to investigate the contact angle profile over time. Every measurement was repeated at least four times.

### 2.2.7 Measurement of interaction forces using an Surface forces apparatus (SFA).

Molecular interactions and the absolute separation distances between two surfaces were measured in an asymmetric system with the Surface Forces Apparatus 2000 (Surforce LLC, Santa Barbara, CA, USA). A freshly cleaved back-silvered mica and gold surface were glued onto each cylindrical glass disc (Radius  $R$ ,  $\sim 2$  cm) using an optical adhesive, Norland optical adhesive 81 (Norland Products, Inc. Cranbury, NJ, USA). The SAMs deposited on the gold layers were placed onto the upper discs. The DSPH phage layer on the back-silvered mica was placed on the lower disc. The two opposing surfaces were arranged with a cross-cylindrical geometry in the SFA chamber, and 50  $\mu\text{L}$  of a 3 mM  $\text{KNO}_3$  solution (pH 3.0 and 8.5) was injected between the surfaces. The SFA chamber was thoroughly sealed and maintained for 30 min after the injection of each solution to achieve equilibration. The contact time ( $t_c$ ) effects were also investigated by taking measurements first at  $t_c = 5$  s and followed by at  $t_c = 1$  h. All measurements were conducted at room temperature ( $T = 23$  °C).

Force vs. distance profiles were measured at a constant rate of 5 nm  $\text{s}^{-1}$ . The normal force  $F$  was calculated as a function of the absolute surface separation distances  $D$  as follows:  $\Delta F(D) = k (\Delta D_{\text{applied}} - \Delta D_{\text{means}})$ , where  $k$  is the double cantilever spring constant of 1225.8 N  $\text{m}^{-1}$ . The distances  $D$  were confirmed from fringes of equal chromatic order (FECO) by using multiple beam interferometry (MBI) in real time. The forces were normalized by their radii ( $R \sim 2$  cm) as  $F_{\text{curved}}(D) R$  for the cylindrical discs. The normalized force  $F/R$  was converted to the interaction energy per unit area  $W$  between the two flat surfaces based on the Derjaguin approximation,  $W_{\text{flat}}(D) = F_{\text{curved}}(D)/2\pi \sqrt{R_1 R_2} = F_{\text{curved}}(D)/2\pi R$ , with  $R_1 = R_2$ . The adhesion energy was obtained using the Johnson-Kendall-Roberts (JKR) model, which is useful for soft materials with large deformations,  $W_{\text{ad}} = 2F_{\text{ad}}/3\pi R$ <sup>50</sup>. Each experiment was repeated, at least three times at the same contact point to investigate hysteresis effect, and at least at three different contact points under the same conditions for reproducibility and repeatability.



### 2.2.8 SWCNT-DSPH phage complexation.

Before complexation with the DSPH phages, SWCNT (HiPCo™, diameter: 0.8–1.2 nm, length: 100–1,000 nm) dispersions were prepared using a 2 wt% sodium cholate surfactant based on a previous report.<sup>42</sup> The DSPH phage and SWCNTs were mixed at a molar ratio of 5:1 (SWCNTs:DSPH phage) with a final concentration of DSPH phages of  $1.0 \times 10^{12}$  pfu mL<sup>-1</sup>. The SWCNT-DSPH solution mixture was first dialyzed against water (10 mM NaCl) at pHs of 3.0, 5.0, and 8.5 for complexation. Dialysis was conducted overnight with frequent solution changes.

## 2.3 Results

### 2.3.1 Experimental set-up and contact angle measurements.

A monolayer of M13 phage (DSPH phage) and functional terminated SAMs were prepared for SFA analysis (Figure 2.2). Atomically flat nature mica substrate was coated with DSPH phage after replacing surface potassium ions with magnesium ions and exposing the substrate to the phage solution (see Methods section for details). AFM confirmed the monolayer deposition of filamentous the DSPH phages with uniform lengths (880 nm) and diameters (6.6 nm) (Figure 2.1), as reported previously<sup>41</sup>. The deposition density of the phage was controlled by varying the concentration of the phage solution. For the SFA analysis, the number density was adjusted to be  $\sim 30$  per  $\mu\text{m}^2$ , because it led to the highest coverage (82%) of the mica surface by the phage without the formation of phage multilayers and aggregates, which can hinder the precise measurement of the interaction forces. In the case of the SAMs, each of the five different end-functionalized alkanethiols was deposited on a molecularly smooth gold surface (Figure 2.2, see Methods section for details).

Prior to the measurement of the interaction forces, the wetting properties of the DSPH phage and the five different functionalized SAMs were investigated as a function of the pH and/or waiting time ( $t$ ) because of their pH-dependent physicochemical properties (Figure 2.3.; see Methods section for more details). Considering the  $pK_a$  values of the functional groups (Table 2.1) and side-chain functional groups of amino acids in DSPH phage (Table 2.2), as well as the isoelectric point (pI) value of the latter ( $\sim 5.3$ )<sup>42</sup>, contact angles were measured at pH 3.0 and 8.5, respectively.

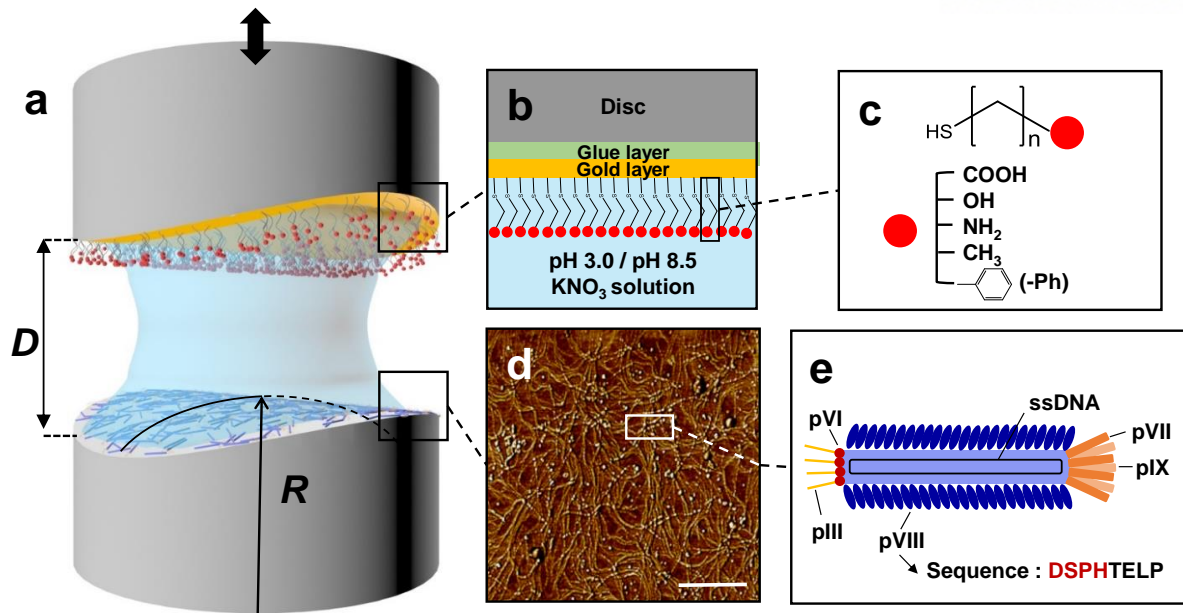


**Figure 2.2.** Experimental Scheme. **a** Surface forces apparatus set-up for measuring interaction forces between the functionalized SAM layer (top surface) and M13 bacteriophage deposited on mica (bottom surface). **b** Functionalized SAM layer on gold surface. **c** Molecular structure of five different alkanethiols for the formation of the functionalized SAM layers. **d** AFM image of M13 bacteriophage on mica. Scale bar, 1  $\mu\text{m}$ . **e** Structure of the M13 bacteriophage.

**Table 2.1.** Properties of the SAMs tested in this study<sup>51-57</sup>.

Functionalized SAMs	pK <sub>a</sub>	Density (molecules/cm <sup>2</sup> )	Thickness (nm)
<i>10-carboxy-1-decanthiol</i> (COOH-SAM)	5.5	$4 \times 10^{14}$	1.25
<i>11-hydroxyl-1-undecanethiol</i> (OH-SAM)	16-18		2.41
<i>11-amino-1-undecanethiol,</i> <i>hydrochloride</i> (NH <sub>2</sub> -SAM)	7.5		1.43
<i>1-undecanethiol</i> (CH <sub>3</sub> -SAM)	-		0.91
<i>2-phenylethanethiol</i> (Ph-SAM)	-	$4.65 \times 10^{14}$	0.85

**Table 2.2.** The  $pK_a$  values of the amino acids in the surface-exposed pVIII protein of the DSPH phage<sup>58</sup>.

<b>Amino acid</b>	<b><math>pK_{a1}</math> (-COOH)</b>	<b><math>pK_{a2}</math> (-NH<sub>3</sub><sup>+</sup>)</b>	<b><math>pK_R</math> (R group)</b>
<i>Aspartate (D)</i>	1.88	9.60	3.65
<i>Serine (S)</i>	2.21	9.15	-
<i>Proline (P)</i>	1.99	10.96	-
<i>Histidine (H)</i>	1.82	9.17	6.00
<i>Threonine (T)</i>	2.11	9.62	-
<i>Glutamate (E)</i>	2.19	9.67	4.25
<i>Leucine (L)</i>	2.36	9.62	-

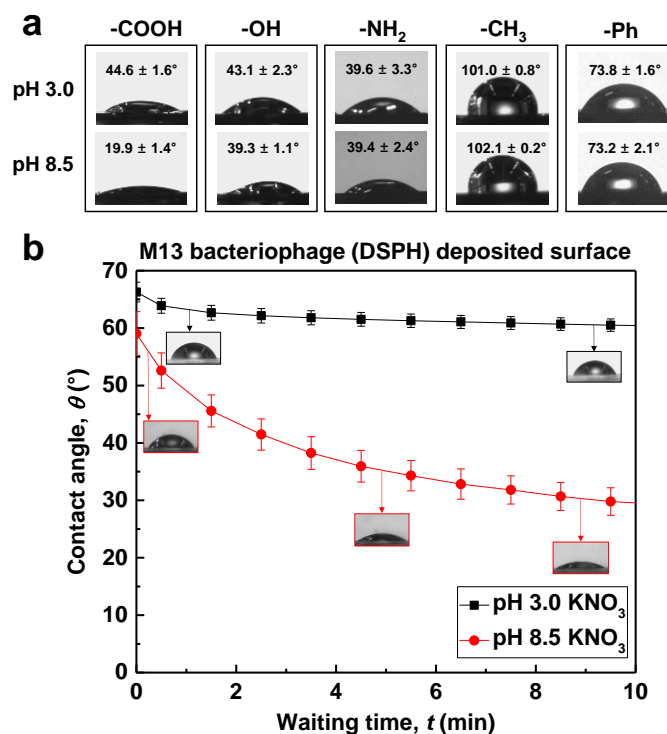


**Figure 2.3.** The wetting properties of the functionalized SAMs and DSPH. Contact angle values of **a** functionalized SAMs and **b** DSPH-coated surface as a function of pH and/or waiting time. The error bars represent the s.e.m. (standard error of mean) where  $n \geq 7$ .

There was not significant different between the contact angles measured at pH 3.0 and 8.5 for most the SAMs (Figure 2.3a). The Ph-/CH<sub>3</sub>-SAM and OH-/NH<sub>2</sub>-SAM remained hydrophobic and hydrophilic, respectively, regardless of the pHs. On the other hand, the COOH-SAM showed significant differences between the contact angles at pH 3.0 ( $\theta = 44.6 \pm 1.3^\circ$ ) and 8.5 ( $\theta = 19.9 \pm 1.4^\circ$ ). Due to its  $pK_a$  value ( $\sim 5.5$ )<sup>53</sup>, it could be deprotonated and become more hydrophilic at pH 8.5. It is noteworthy that the NH<sub>2</sub>-SAM should also be pH sensitive ( $pK_a \sim 7.5$ ), but it exhibited a negligible difference in the contact angles upon pH changes<sup>52</sup>. The observed difference in the pH-dependent wetting properties of the COOH- and NH<sub>2</sub>-SAMs can be attributed to the differences in their molecular conformations. The NH<sub>2</sub>-SAM can form hydrogen bonding networks with surrounding water molecules, regardless of its protonation state<sup>59, 60</sup>. However, the COOH-SAM can form intermolecular hydrogen bonding between end functional groups only when they are protonated, leading to the decrease in the hydrophilicity with the pH<sup>61, 62</sup>.

The wettability of the DSPH phage coated surface was measured as a function of the pH and waiting time ( $t$ ) after contact with the solution to determine the rearrangement/reorientation of the coat-proteins of the phage on the mica surface (Figure 2.3b). The contact angle at pH 8.5 gradually decreased from  $\theta = 59.1 \pm 3.8^\circ$  ( $t = 0$  s) to  $\theta = 27.1 \pm 0.6^\circ$  ( $t = 10$  min). The contact angle at pH 3.0

was relatively insensitive to the waiting time, showing a slight decrease  $\theta = 66.3 \pm 1.7^\circ$  ( $t = 0$  s) to  $\theta = 60.4 \pm 1.1^\circ$  ( $t = 10$  min). Considering its pI value ( $\sim 5.3$ ), the positively charged DSPH phage at pH 3.0 could interact more strongly with the negatively charged mica surface than with water molecules, resulting in a slightly high contact angle and a negligible change over time. However, significant amounts of negatively charged amino acids (e.g. aspartic acid and glutamic acid) in the DSPH phage could reorient and become exposed to the DSPH phage-water interface, increasing the hydrophilicity with time. In addition, swelling of the DSPH phage (which was deduced by SFA experimental part, as presented in a later section) could increase the rotational degrees of freedom, which may have accelerated the rearrangement process<sup>63, 64</sup>.

### 2.3.2 Interaction force measurements.

In addition to evaluating the hydrophobicity/hydrophilicity of DSPH phage and the five different functional terminated SAMs, the interaction forces between the DSPH phage and the five different SAMs were measured using SFA (Figure 2.4 and 6). Force *vs.* distance profiles were measured upon approach and detachment of DSPH phage- and SAM-modified surfaces to determine the adhesion force and energy ( $W_{ad}$ ) under various conditions : pHs of 3.0 and 8.5 and contact times ( $t_c$ ) of 5 s and 1h.

The interaction forces at pH 3.0 was measured firstly. The adhesion energy between the COOH-SAM and DSPH phage increased from  $W_{ad} = 0.23 \pm 0.02$  mJ m<sup>-2</sup> at  $t_c = 5$  s to  $W_{ad} = 2.32 \pm 0.40$  mJ m<sup>-2</sup> at  $t_c = 1$  h (Fig. 3a). The OH-SAM increased from  $W_{ad} = 3.08 \pm 0.75$  mJ m<sup>-2</sup> at  $t_c = 5$  s to  $W_{ad} = 5.32 \pm 0.26$  mJ m<sup>-2</sup> at  $t_c = 1$  h (Figure 2.4b). The similar contact angles of the COOH - ( $\theta = 44.6 \pm 1.6^\circ$ ) and OH-SAMs ( $\theta = 43.1 \pm 2.3^\circ$ ) at pH 3.0 suggest that should they have similar magnitudes of hydration repulsion or hydrophobic attraction. Despite the expected similarity in the origin of adhesion for both SAMs (e.g. hydrogen bonding), the measured adhesion energy of the COOH-SAM was  $\sim 30\text{--}50\%$  smaller than that of the OH-SAM. This quantitative discrepancy is attributed to the differences in the molecular conformation of their terminal functional groups in aqueous solutions. As mentioned in previous part, the protonated carboxylic head group (-COOH) at pH 3.0 can partially form a hydrogen bonding with a neighboring group (-H with -O-) or a dimer (-H with =O)<sup>61</sup>. It suggests that the DSPH phage may have fewer changes to form hydrogen bonding with the protonated COOH-SAM than with the OH-SAM at pH 3.0, which also coincides with a molecular dynamics simulation study<sup>65</sup>.

The adhesion energy between NH<sub>2</sub>-SAM and DSPH phage ( $W_{ad} = 4.30 \pm 0.29$  mJ m<sup>-2</sup> at  $t_c = 1$  h) was comparable to that between the OH-SAM and the phage despite the positive charges of them at pH 3.0 (Figure 2.4c). It was expected that hydrogen bonding would occur between the NH<sub>2</sub>-SAM and DSPH phage, as both are rich in hydrogen bonding donors and acceptors. Moreover, it was predicted that additional interactions would be present because the measured force *vs.* distance profile indicated that

electrostatic repulsion between them was negligible compared to the adhesion forces. It is well known that protonated primary amines can have cation- $\pi$  interactions as a cationic donor with aromatic moieties, such as histidine of the pVIII protein. Assuming that half of the pVIII proteins from the deposited phages participated in these interactions, the adhesion force per pVIII protein would be roughly  $15.3 \text{ kcal mol}^{-1}$  ( $\sim 26 kT$ ). It suggests that there could be multiple cation- $\pi$  interactions per pVIII protein because the strength of the cation- $\pi$  interaction was estimated to be  $\sim 5.5 \text{ kcal mol}^{-1}$  in water<sup>66</sup>.

The adhesion energy between the CH<sub>3</sub>-SAM and DSPH phage layer was significantly higher ( $W_{\text{ad}} = 7.00 \pm 0.10 \text{ mJ m}^{-2}$ ) compared to those of the COOH-, OH-, and NH<sub>2</sub>-SAMs (Figure 2.4d). The origin of the strong attraction between the DSPH phage and CH<sub>3</sub>-SAM was most likely due to the strong *hydrophobic interactions*, as evidenced by the contact angle value, indicating that the CH<sub>3</sub>-SAM was very hydrophobic ( $\theta = 101.0 \pm 0.8^\circ$ ). The approach curve indicates that any types of repulsive forces were completely overwhelmed by the strong adhesion until the surfaces became closer than their steric wall distance,  $D_{\text{sw}}$  (Figure 2.5d)<sup>11</sup>. A simple DSPH phage adsorption experiment on the CH<sub>3</sub>- and COOH-SAM perfectly corresponded with the SFA result, which describe the deposition of a significantly denser DSPH phage layer on the CH<sub>3</sub>-SAM compared to the COOH-SAM (Figure 2.5).

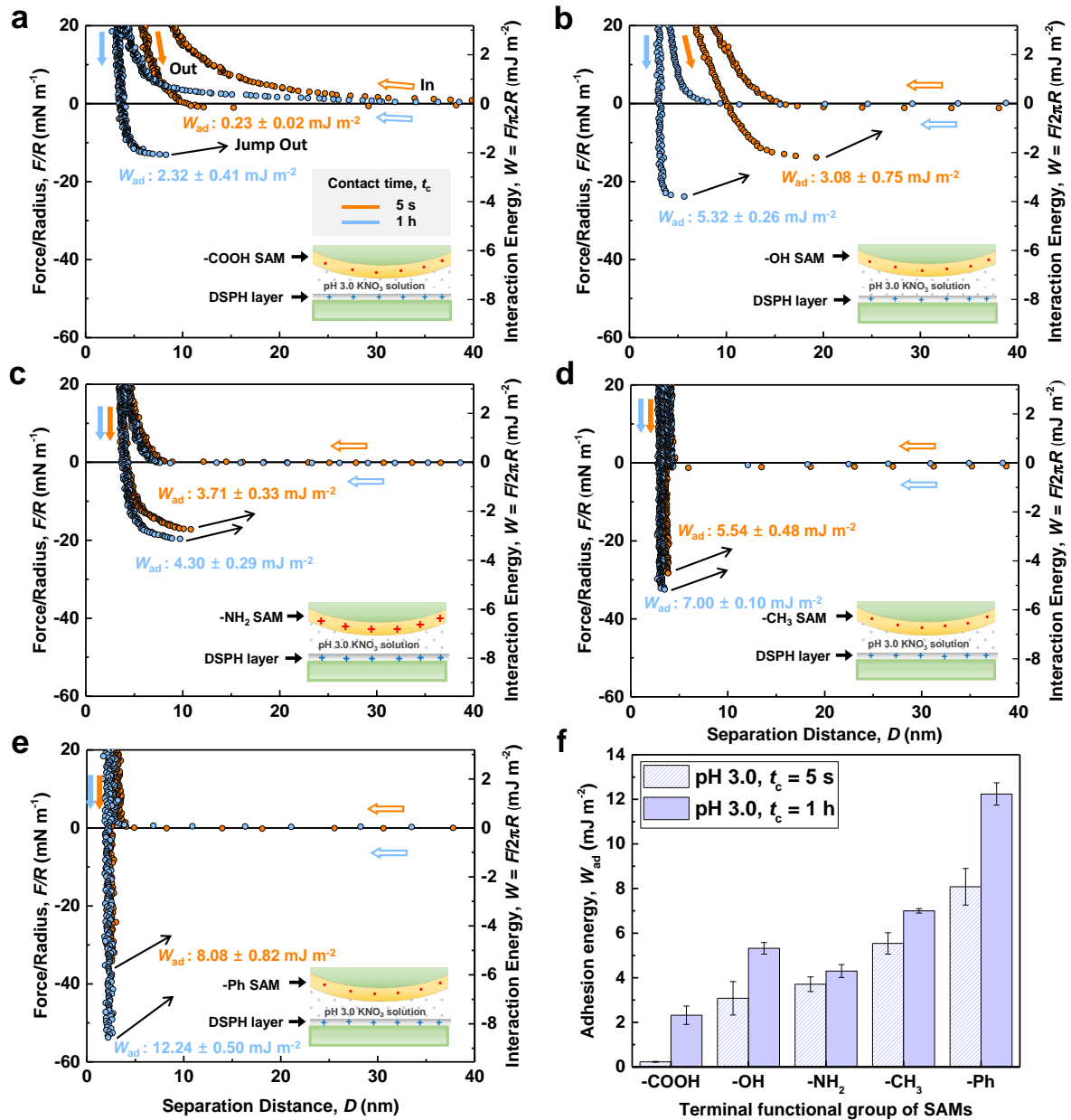


**Figure 2.4.** Force vs. distance profiles measured at pH 3.0. The interactions force of the DSPH-coated surface was measured against SAMs with five different terminal functional groups: **a** -COOH, **b** -OH, **c** - $\text{NH}_2$ , **d** - $\text{CH}_3$ , and **e** -Ph. The empty and solid arrows correspond to the approach and detachment of the two surfaces, respectively. The orange and sky-blue curves correspond to the force-profiles at contact times ( $t_c$ ) of 5 s and 1 h, respectively. **f** Bar-graph showing the overall adhesion energy ( $W_{ad}$ ) of different SAMs at pH 3.0 as a function of contact time. The error bars represent the s.e.m. where  $n = 5$  in each group.



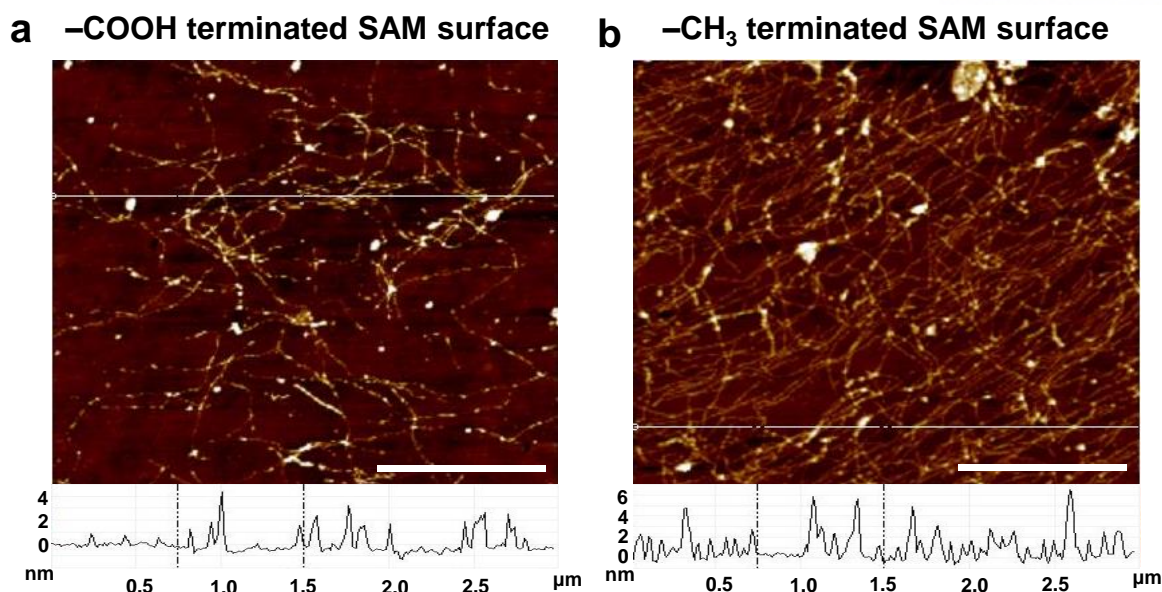


**Figure 2.5.** AFM images showing the influence of the terminal functional groups on the molecular interactions between the DSPH bacteriophages and the SAMs. **a** COOH-terminated and **b** CH<sub>3</sub>-terminated SAMs. The concentration of the DSPH phage solution was maintained at  $2.74 \times 10^{12}$  pfu mL<sup>-1</sup>. Scale bar is 1 μm.

Among all the tested functionalized SAMs, the Ph-SAM exhibited the highest adhesion energy against the DSPH phage at pH 3.0 ( $W_{\text{ad}} = 8.08 \pm 0.82$  mJ m<sup>-2</sup> at  $t_c = 5$  s and  $W_{\text{ad}} = 12.24 \pm 0.50$  mJ m<sup>-2</sup> at  $t_c = 1$  h) (Figure 2.4e). If the strong adhesion between the phage and Ph-SAM was solely caused by hydrophobic interactions, the adhesion energy between them should be lower compared to that between the phage and CH<sub>3</sub>-SAM, as the CH<sub>3</sub>-SAM was more hydrophobic, as shown in Figure 2.3. Hence, the strong interactions between the DSPH phage and Ph-SAM can be attributed to the  $\pi$ - $\pi$  stacking (as hypothesized from other work), cation- $\pi$ , and hydrophobic interactions. The high proportions of histidine (H) and proline (P) in the surface-exposed portion of the pVIII protein (DSPHTELP) for the DSPH phage (~12.5 and ~25%, respectively) were closely correlated to these results. It was reported that even though proline is not a  $\pi$  conjugated system at pH 3.0, it can favorably interact with the  $\pi$ -electron-rich phenyl aromatic face and induce the aforementioned interactions, minimizing the steric penalty<sup>67</sup>.

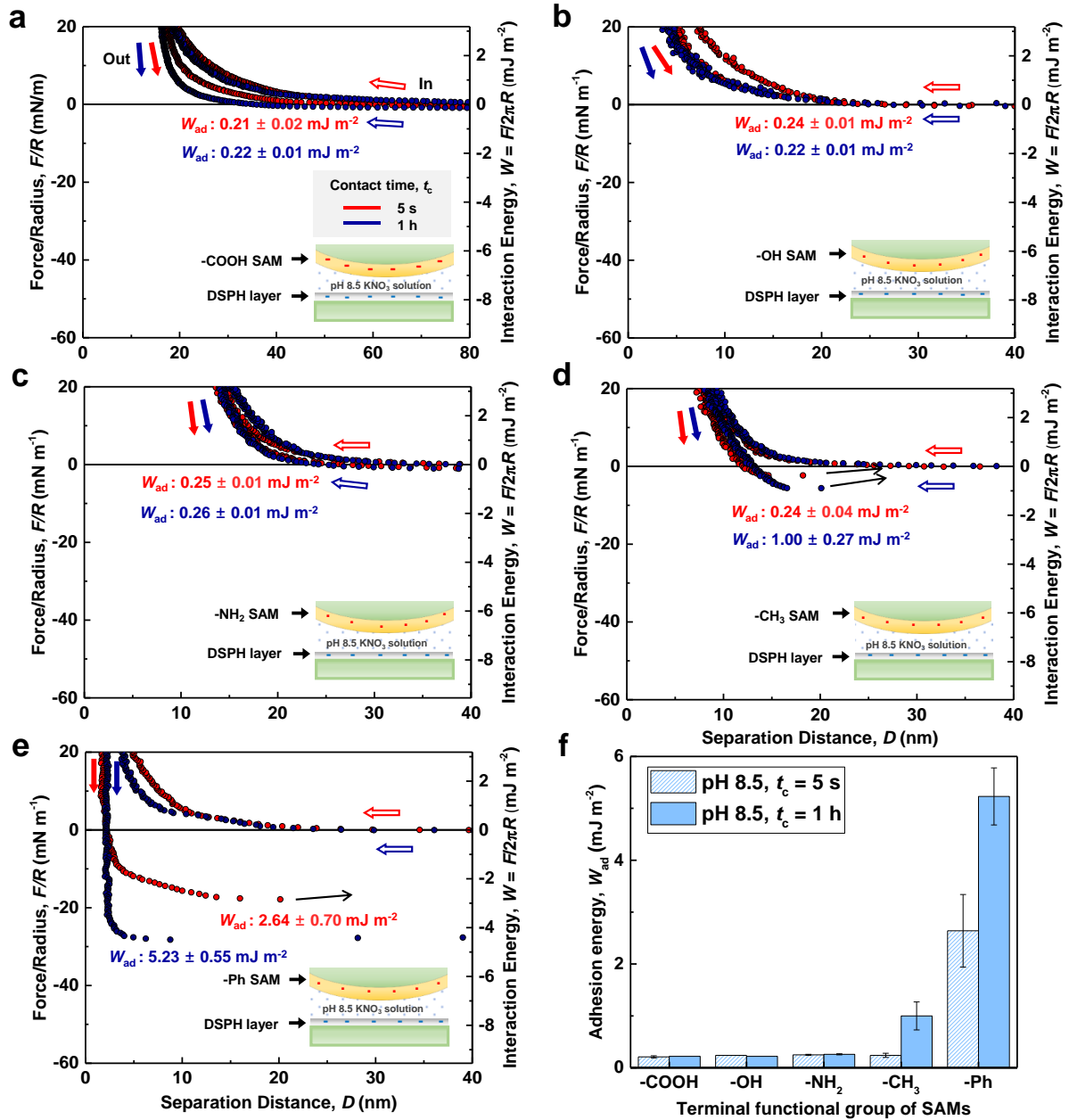


**Figure 2.6.** Force vs. distance profiles measured at pH 8.5. The interactions force of the DSPH-coated surface was measured against SAMs with five different terminal functional groups: **a** -COOH, **b** -OH, **c** -NH<sub>2</sub>, **d** -CH<sub>3</sub>, and **e** -Ph. The empty and solid arrows correspond to the approach and detachment of the two surfaces, respectively. The red and blue curves correspond to the force-profiles at contact times ( $t_c$ ) of 5 s and 1 h, respectively. **f** Bar-graph showing the overall adhesion energy ( $W_{ad}$ ) of different SAMs at pH 8.5 as a function of contact time. The error bars represent the s.e.m. where  $n = 5$  in each group.

Previous studies showed that the magnitude of the  $\pi$ - $\pi$  stacking energy mediated by protonated

histidine is stronger than that of deprotonated histidine<sup>68</sup>. In biological systems, the positively charged histidine has been known to be an important cationic source in cation- $\pi$  interactions for regulating protein folding and reactivity<sup>69</sup>. Considering that histidine is always protonated under acidic conditions (pH 3.0), cation- $\pi$  interactions would be one of the major contributors to the interactions with the Ph-SAM. Furthermore, all the amino acids'  $\alpha$  protons could interact with the Ph-SAM via CH/ $\pi$  interactions, regardless of the pH conditions<sup>67</sup>.

All the adhesion energies measured at pH 3.0 were higher at  $t_c = 1$  h compared to those at  $t_c = 5$  s. The increase in adhesion with  $t_c$  is a typical sign of structural rearrangements or reorientation of biological macromolecules<sup>50, 70</sup>, indicating that the adhesive bonds (physical interactions including van der Waals, H-bonding, and hydrophobic attraction in this study) developed favorably while the functional groups and DSPH were in contact. The decrease in  $D_{sw}$  during contact also supports that molecular rearrangement occurred (Figure 2.7).

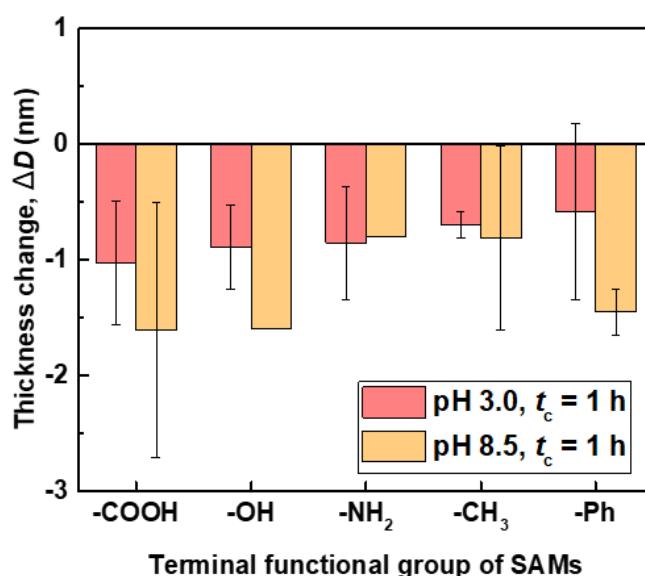


**Figure 2.7.** Change in the thicknesses ( $\Delta D$ ) of the SAMs before and after contact with the DSPH phage-coated surface for 1 h. The observed decrease in thicknesses ( $\Delta D < 0$ ), irrespective of types of the terminal functional groups, indicated that rearrangement or reorganization of the coat-proteins in the DSPH phage occurred over time. The error bars represent the s.e.m. ( $n = 5$  in each group).

In general, the adhesion energies at pH 8.5 were much lower than those in the acidic condition (pH 3.0) were, regardless of the opposing functional group (Figure 2.6). The increase in the hydrophilicity of the DSPH phage-coated surface (as shown in the contact angle measurements) and the larger  $D_{sw}$  between the two opposing layers indicate the existence of strong steric- and hydration-repulsion caused by the swelling of the phages on the mica surface.

Consequently, for the COOH-, OH-, and NH<sub>2</sub>-SAMs, repulsive forces dominated over all the other adhesive forces, yielding purely repulsive force vs. distance profile. On the other hand, for the CH<sub>3</sub>- and Ph-SAM, the adhesive forces were still stronger than the repulsive counterparts were, even though significant decreases in the adhesion energies were observed at pH 8.5. The adhesion energies between the Ph-SAM and DSPH phage layer ( $\sim 2.64 \pm 0.70 \text{ mJ m}^{-2}$  at  $t_c = 5 \text{ s}$  and  $\sim 5.23 \pm 0.55 \text{ mJ m}^{-2}$  at  $t_c = 1 \text{ h}$ ) were still the strongest (Figure 2.6e), indicating the dominance of  $\pi$ - $\pi$  interactions due to the histidine and CH/ $\pi$  interactions induced by proline in the DSPH phage<sup>67</sup>. The plateau before the ‘jump-out’ upon the detachment of the Ph-SAM (Figure 2.6e) at pH 8.5, which was absent at pH 3.0, may indicate that highly hydrated residues of the DSPH phage were ‘peeled-off’ before detachment (Figure 2.8.).

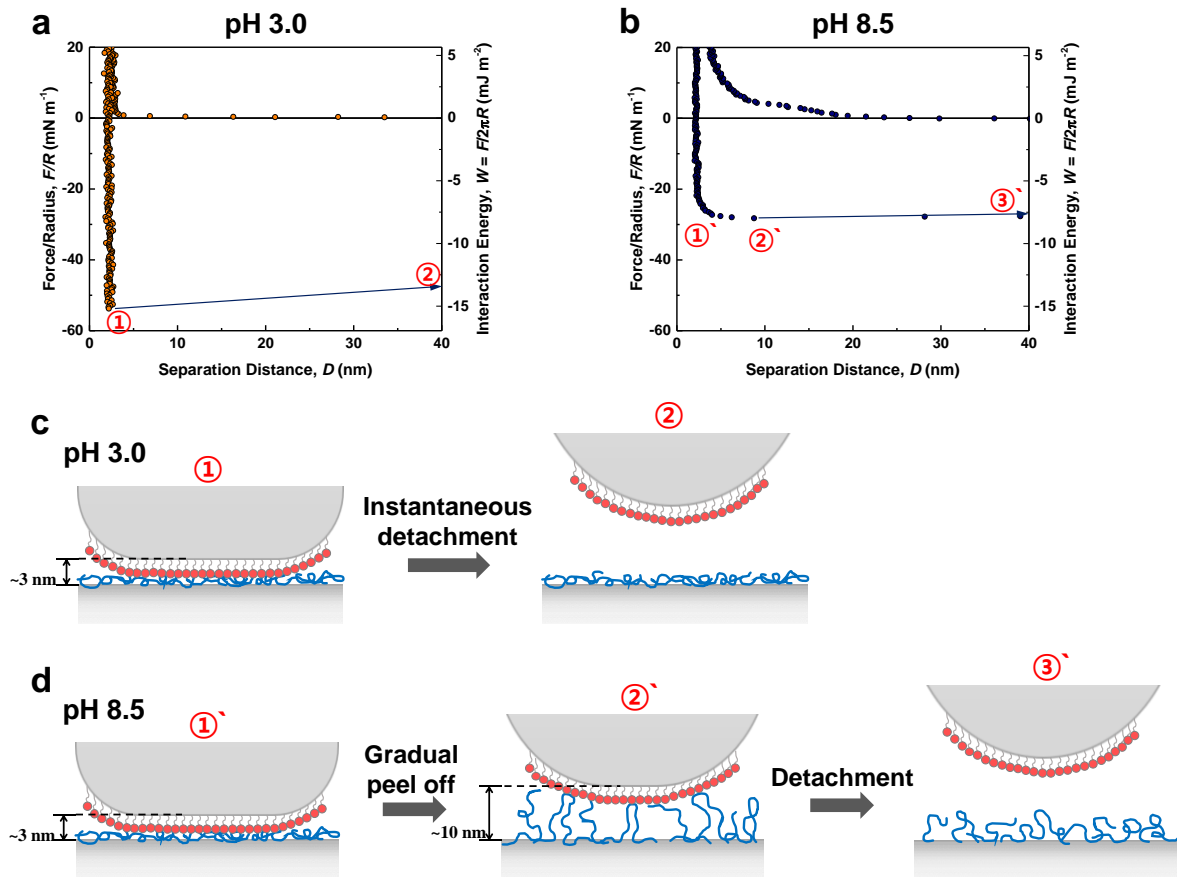


**Figure 2.8.** Force-distance profiles of Ph-SAM vs. DSPH-coated surface,  $t_c = 1 \text{ h}$ . **a** at pH 3.0 and **b** at pH 8.5 **c** Instantaneous detachment was observed from ① to ② at pH 3.0, while **d** gradual peel off was observed from ①' to ②' at pH 8.5 until ③' final detachment.

The adhesion energy per virus can be calculated based on the number density of DSPH phage on the MgCl<sub>2</sub> treated mica surface (calculated from AFM images) and the measured  $W_{ad}$ . Compared to the

known dimension of DSPH phage (diameter  $\sim 6.5$  nm)<sup>43</sup>, adsorbed DSPH phage in AFM image (Figure 2.2) seems to be in a “compressed cylinder” shape (lateral thickness  $\sim 20$  nm) rather than a normal cylinder. Thus, 50% is a reasonable upper bound of the pVIII protein fraction directly involved in adhesion. Especially, the adhesion energy per DSPH phage on the Ph-SAM was  $\sim 4.2 \times 10^{-16}$  J (at pH 3.0 and  $t_c = 1$  h), which corresponds to  $\sim 10^5 kT$  at room temperature. Considering the number of pVIII proteins per M13 phage ( $\sim 2,700$  copies)<sup>71</sup>, with the assumption that about 50% of the pVIII proteins were involved in the adhesion, the adhesion energy per pVIII protein was  $\sim 74 kT$ . It is noteworthy that this value is significantly higher than the adhesion energy of well-known mussel foot proteins; the adhesion energy between a 25-mer-long mussel foot protein-3s and the hydrophobic surface was estimated to be  $\sim 34.7 kT$  by replica-exchange molecular dynamics (REMD) simulations.<sup>72</sup> Using the same assumption, the adhesion energy of one pVIII against the Ph-SAM was calculated to be  $\sim 32 kT$  at pH 8.5.

### 2.3.3 Complexation and dispersion of SWCNT using DSPH phage.

Based on the result that DSPH phage strongly interacts via  $\pi$ - $\pi$  interaction, I investigated the pH-dependent properties of single-walled carbon nanotubes (SWCNT) and DSPH phage complexes. The DSPH phage was reported to strongly bind with SWCNT and maintain a stable dispersion state without re-bundling<sup>42, 43</sup>, enabling diverse applications including *in vitro* and *in vivo* bioimaging and synthesis of CNT-based hybrid materials in aqueous solutions. However, the underlying mechanisms for their complexation and dispersion stability is less known. However, little is known about the underlying mechanism for their complexation and dispersion stability, especially at high CNT concentrations. The complexation was conducted through the dialysis of a surfactant-assisted SWCNT dispersion in the presence of the DSPH phage at three different pHs (pH 3.0, 5.0, and 8.0).

Possible interactions between the DSPH phage and SWCNTs are described in Fig. 5a as a function of pH. It was anticipated that  $\pi$ - $\pi$  stacking and hydrophobic interactions were always present, regardless of the pH values. At a low pH, cation- $\pi$  and electrostatic interactions may be additionally present. Due to the presence of only attractive interactions at pH 3.0 and 5.0, the dialysis of the complexing solution resulted in the formation of hazy aggregates (Figure 2.9b). It seems to be contrary to previous studies that found the formation of stable SWCNT-DSPH complexes under similar conditions<sup>42, 43</sup>. Note that I have used a much higher concentration of DSPH phage and SWCNTs for their complexation than previous studies; their high concentrations can decrease the separation distance and help overcome (repulsive) kinetic barriers to achieve thermodynamic equilibrium, allowing the facile acquisition of the (aggregated) global minimum state. However, the formation of any aggregates for the sample prepared at pH 8.5 could not be observed. The resulting SWCNT-DSPH complex solutions remained stable over six months without any noticeable

precipitation or change. The observed high dispersion stability of the SWCNT-DSPH complexes was attributed to the presence of additional electrostatic repulsive interactions between the complexes. The repulsive interactions can rise from negatively charged amino acids on the DSPH phage (e.g., glutamic acid and aspartic acid) and dominate over other short-range attractive interactions (e.g.,  $\pi$ - $\pi$  stacking and hydrophobic interactions). The complex solutions were analyzed by AFM to observe the morphology of the SWCNT-DSPH complex in detail (Figure 2.9c). AFM imaging and cross-section analyses showed severe aggregation of the DSPH phages and SWCNTs at pH 3.0. It suggests that  $\pi$ - $\pi$  stacking and hydrophobic interactions were the main driving forces for the binding of the DSPH phages with the SWCNTs, which correlated well with the SFA results. At higher pHs, the phages became negatively charged due to the deprotonation of glutamic acids and aspartic acids in the pVIII protein, increasing the electrostatic repulsion between the phages and phage-bound SWCNTs. Hence, the degree of repulsion was a major factor that affected the dispersion stabilities of the SWCNT-DSPH phage complexes. Consequently, the aggregate formation and dispersion of SWCNTs can be simply tuned by the pH conditions when using the DSPH phages as a dispersant.

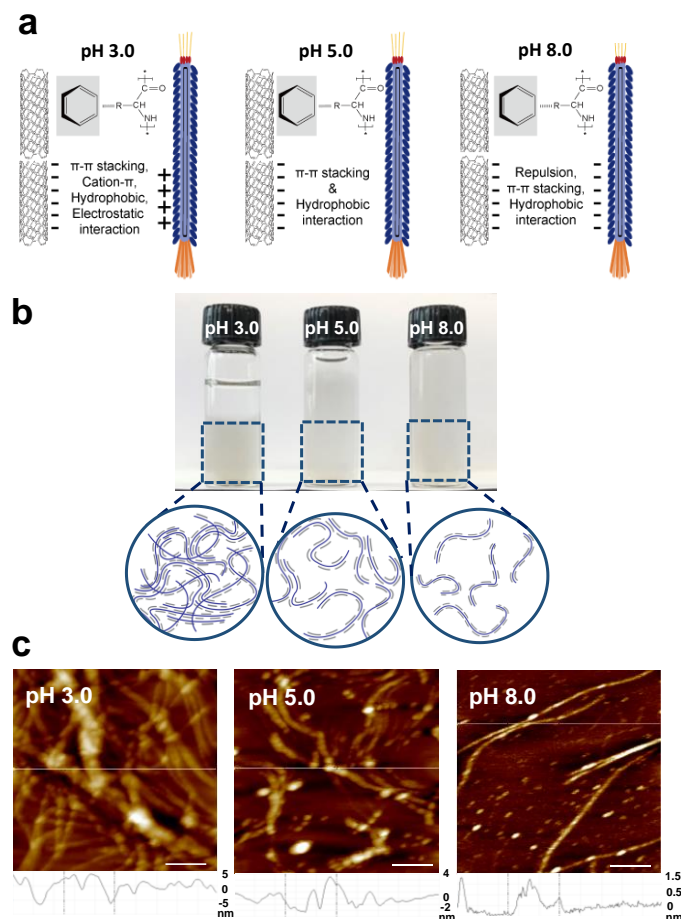


**Figure 2.9.** Dispersion stability of SWCNT-DSPH complex at different pHs. **a** Graphical illustration showing a list of potential interactions between the DSPH phages and SWCNTs upon their complexation. **b** Photographs of SWCNT-DSPH phage complexes prepared at different pHs: 3.0, 5.0,

and 8.5. Schematic illustration explaining the observed difference in their dispersion stabilities. **c** The corresponding AFM images of SWCNT-DSPH phage complexes. Scale bar, 100 nm.

### 2.3.4 Discussion

Although the highly logical and reliable results, a few issues that should be addressed in the future studies remain. First, I cannot completely exclude the possibility that another portion of the DSPH phage (e.g. pIII or pVIII) other than the exposed pVIII sequences participated in the interactions with the SAMs. Second, it would be useful to measure the interaction forces of various point-mutated phages for a more straightforward and systematic investigation of the origin of the molecular recognition capabilities. More ideally, solid phase synthesized short peptides can apply rather than the whole phage. Nevertheless, I believe that the present study can provide insights and solid foundations for studies on specific interactions of biomolecules.

### 2.4 Conclusion

Using a model biomolecule (e.g. pVIII peptides sequence on M13 phage) and the functionalized SAMs, the possible interaction forces and strengths precisely identified and qualified. I found that histidine and proline moieties may perform a critical role in the molecular recognition of SWCNT by the DSPH phage though their engagement in attractive  $\pi$ -interactions, as expected previously, and additionally through hydrophobic interactions. The measured strength of each identified interaction was comparable to previously reported values<sup>42</sup>. It is thought that a much higher abundance of pVIII protein at the phage surface compared to other proteins allowed the SFA analysis with adequate reliability. In addition, I experimentally demonstrated that DSPH-SWCNT complexes can be stabilized at high pH through electrostatic and hydration repulsion.

The interaction origin of M13 bacteriophage (DSPH phage) was investigated by directly measuring interaction forces against the functionalized SAMs (-COOH, -OH, -NH<sub>2</sub>, -CH<sub>3</sub>, and -Ph). The overall results indicated that the DSPH phage exhibited the highest and lowest adhesion energy with the phenyl and carboxylic acid group respectively, indicating that the phages strongly interacted via  $\pi$ - $\pi$  stacking and hydrophobic interactions, while the H-bonding interactions remained relatively weak. Moreover, I confirmed that DSPH phages interacted strongly with the SWCNTs in acidic conditions via the physical interactions mentioned previously. Hence, pH-responsive tuning of the M13 bacteriophage-SWCNT complexes is possible. The obtained results can be used as a fundamental database in bacteriophage-based applications to enhance the performance of future phage-based templates. Furthermore, the utilized measurement protocol, using functionalized SAMs as opposing surfaces, can be applied to study the molecular interaction mechanisms of various bio and synthetic materials.

## Chapter 3. Investigation of adhesion mechanisms in CNT-binding peptide

### 3.1 Introduction

Many identified diseases are induced at the protein level, so most medicines are developed to detect target proteins<sup>73, 74</sup>. It is essential to understand protein-ligand and protein-protein interactions for effective drug development<sup>1, 75, 76</sup>. The interactions play important roles in tracking disease states in biological systems<sup>77</sup>. Hence, if protein functions and signaling network analysis are understood, it is possible to design molecules that promote or inhibit specific interactions between biomolecules, and thus discover effective disease treatment and prevention methods.

One typical application for specific protein detection is a biosensor<sup>78, 79</sup>. Biosensors have been used in a wide range of fields such as medicine, environment, and food due to their ability to selectively detect and react with specific chemicals. However, in the meantime, detecting biomaterials requires lots of samples and complex analysis steps including inputting analytes, generating signals, and amplifying signals. Recently, research on biosensor devices that can detect small amounts of chemicals have been conducted to overcome the difficulties<sup>80</sup>. The most representative research is a carbon nanotube (CNT) based biosensor that detects chemicals through electrochemical changes in CNT bonded biomaterials<sup>81</sup>. The CNT has electrical and structurally stable properties that are useful for use in biosensors<sup>81</sup>. Additionally, CNT has the advantage of not requiring labeling and allowing the reaction to proceed in aqueous solutions without modifying the protein<sup>82</sup>.

In this work, the interactions of the DSPHTELP peptide sequence, known as a CNT-binding peptide sequence, was measured and quantified by using SFA. Then, the effects of each amino acid on the DSPHTELP sequence are analyzed in interactions with three functional groups (carboxyl, methyl, amine and Phenyl). Based on the results, it is possible to derive and establish the peptide sequence that reliably binds with CNTs via non-specific interactions (non-covalently functionalized CNT) for CNT-based biosensors to detect the desired biomolecules. Therefore, it suggests the interaction factors for designing the CNT-based biosensors which detect specific peptides or proteins.

### 3.2. Experimental section

#### 3.2.1 Material

SWCNT powder were purchased from Sigma Aldrich ( $\geq 89\%$  carbon basis ( $\geq 99\%$  as carbon nanotubes)). The functional terminated alkanethiols, including 10-carboxy-1-decanethiol (95%), 1-undecanethiol (98%), 11-amino-1-undecanethiol, hydrochloride (99%), and 2-phenylethanethiol (98%), were purchased from Sigma-Aldrich.



### 3.2.2. Synthesis of peptide

Short peptide sequence (amino acid sequence : DSPHTELP) was synthesized by the standard 9-fluorenylmethoxycarbonyl solid-phase peptide synthesis on a 0.106 mmol scale. Fmoc-Asp(OtBu)-OH, Fmoc-Ser(tBu)-OH, Fmoc-pro-OH, Fmoc-His(Trt), Fmoc-Thr(tBu)-OH, Fmoc-Glu(OtBu), Fmoc-Leu-OH was used to synthesize peptide sequence. Each amino acid were treated with 1 *O*-(Benzotriazol-1-yl)-*N,N,N',N'*-tetramethyluronium hexafluorophosphate(HBTU)(500  $\mu$ mol) in presence of diisopropyl ethyl amine (DIPEA, 500  $\mu$ mol) and allowed to stir at room temperature for 2 h in DMF. Fmoc group was removed with 3-4ml of 20% piperidine in DMF. The resin was collected by filtration and washed with dimethylformamide (DMF) to remove unreacted chemicals. The product cleaved from the resin with cleavage cocktail (TFA/Water/Tri isopropyl amine mixture (9.5: 0.5: 0.5)) and products were precipitated in cold ether. The crude products were purified by high-performance liquid chromatography (HPLC, Agilent Technologies, USA) with a C18 reverse column in ACN/Water mixture and confirmed by mass analysis using MALDI-TOF/TOF.

### 3.2.3. Synthesis of triethoxysiloxane capped peptide

The structure of triethoxysilane capped DSPHTELP peptide was adopted in order to form the peptides layer on the mica surface. The triethoxysilane induce condensation with hydroxyl group of the O<sub>2</sub> plasma treated mica surface. Therefore, increase attachment ability for mica surface can be achieved by using the siloxane capped DSPHTELP peptide. The synthesized DSPHTELP peptide sequence (50mg, 0.056mmol) was dissolved in dry DMF (1mg/mL). 3-(Triethoxysilyl)propyl isocyanate (13.85mg, 0.056mmol) was added to above solution. After stirring at room temperature for overnight, the mixture was filtered and the residue was purified by size exclusion chromatograph.

### 3.2.4. Preparation of peptide layer on mica surface

For pre-surface treatment for SFA experiments, freshly cleaved muscovite mica layer (Grade #1, S&J Trading, Floral Park, NY, USA) was prepared to a cylindrical glass disc (Radius,  $R \sim 2$ cm) by an UV glue, NOA 81 (Norland Products, Inc. Cranbury, NJ, USA) followed by UV treatment for 1 h.

To prepare the triethoxysiloxane capped peptide surface, the mica surface was treated oxygen plasma process at 100 W,  $50 \times 10^{-1}$  Torr for 3 min. And then, the plasma treated mica was immersed into 20 mL of DMF solution. The 50  $\mu$ L of peptide/DMF solution diluted from 1 mg/ml to 0.005 mg/mL was dropped into the DMF solution at 700 rpm for 1 h. After condensation reaction (Figure 3.2), the surface was rinsed with DMF solution to remove unbound molecules and dried with nitrogen gas. The reaction was performed in nitrogen bench where the humidity is 10-20%.

### **3.2.5. Preparation of end-functionalized self-assembled monolayer**

It is equal to section 2.2.2

### **3.2.6. Measurements of adhesion force using Surface forces apparatus (SFA)**

Molecular interactions and the absolute separation distances between peptide and functional groups (or SWCNT) were measured with the Surface Forces Apparatus 2000 (Surforce LLC, Santa Barbara, CA, USA). The two opposing surfaces were arranged with a cross-cylindrical geometry in the SFA chamber, and 50  $\mu$ L of a 3 mM pH 3.0  $\text{KNO}_3$  solution was injected between the surfaces. The process after this is equal to the section 2.2.7.

## **3.3. Results**

### **3.3.1. Synthesized peptide**

The molecular weight of the synthesized peptide in section 3.2.2. was confirmed by MALDI-TOF. In Figure 3.1, the 916.46 peak is the peak that corresponds to the DSPHTELP peptide sequence. The molecular weight of the peptide is 894.94 g/mol, but a sodium ion binds to the peptide when measuring the molecular weight via the MALDI-TOF used in this work. The 916.46 peak is much higher than other peaks, so the peptide is a major product of the method in section 3.2.2.

The purity of the synthesized peptide was measured via analytical HPLC. The peptide peak is at 11.880 min, and the purity of the peptide was calculated by integrating the peak area (Figure 3.1b). According to the process, the purity of the peptide is over 95%. In addition, the peptide morphology was identified by Bio-TEM (acceleration voltage:120 kV, JEM-1400, JEOL). The peptides appear to have a fibrous form and aggregate with each other without regularity. Hence, it indicates that the repulsion between peptides is weak, and they can bind to each other by non-covalent interactions such as hydrophobic, hydrogen bonding, and van der Waals interactions.

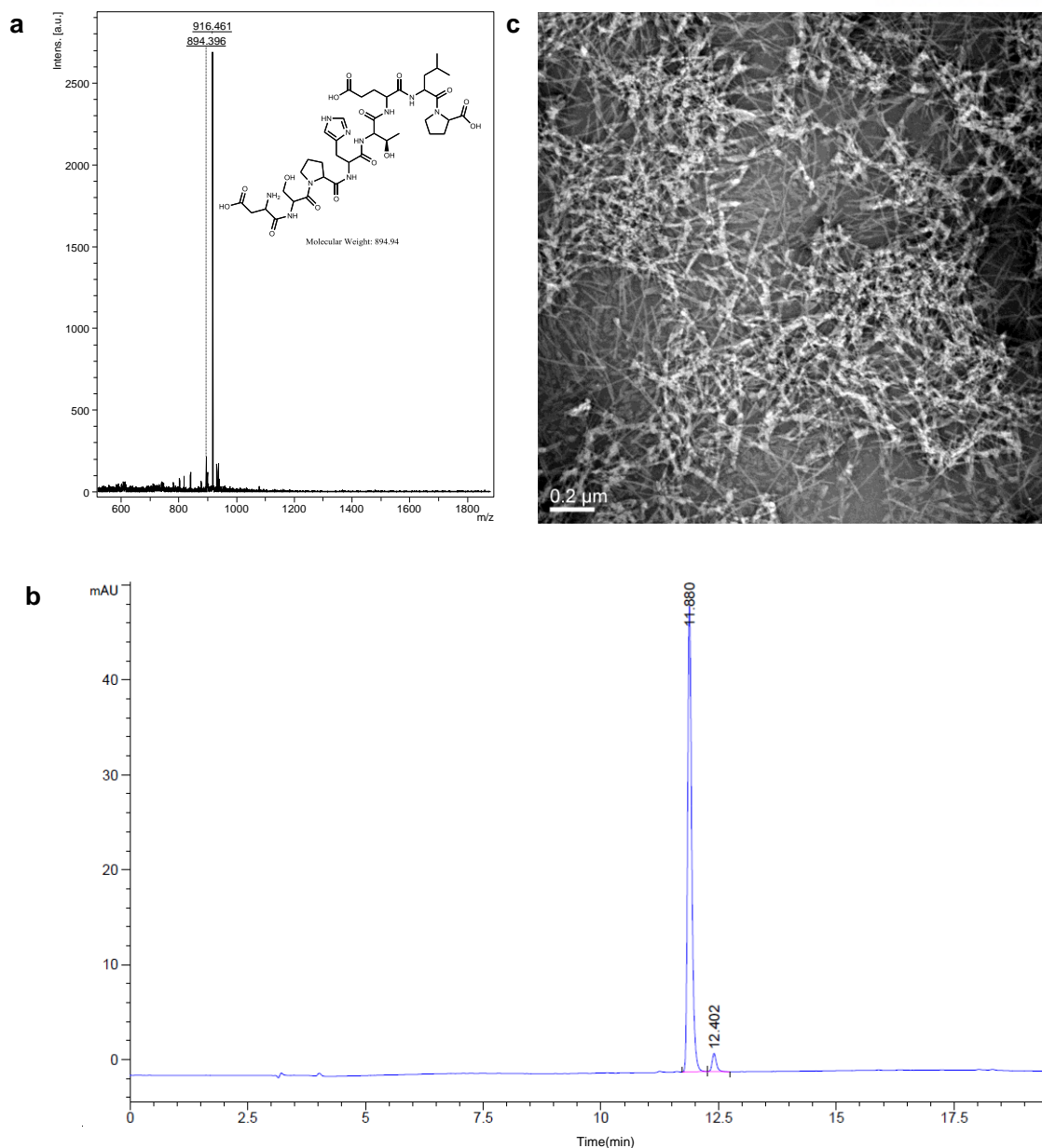


**Figure 3.1.** Analyzed results of the synthesized DSPHTELP peptide sequence analyze. **a** MALDI-TOF **b** HPLC for the purity of refined peptide. **c** Bio-TEM image of the DSPHTELP peptide on the TEM grid.

### 3.3.2. Formation of a peptide layer on mica substrate

The triethoxysiloxane capped DSPHTELP peptide synthesized in section 3.2.3 binds on  $O_2$  plasma treated mica substrate. The peptides evenly bind on the mica substrate, as observed in the surface morphology analysis through AFM (Figure 3.2b). Therefore, the process in section 3.2.4 provides a suitable surface for measuring adhesion forces between peptides and functionalized SAMs.

The contact angle of the peptide layer on mica was measured with a pH 3.0 KNO<sub>3</sub> solution, which is used in the SFA measurement. The angle is  $17.29 \pm 3.52^\circ$ , and the hydrophilicity of the peptide layer surface is caused by the amide groups connected to the N-terminus of the peptide. Unlike the contact angle of the DSPH phage,  $\theta = 66.3 \pm 1.7^\circ$  ( $t = 0$  s) to  $\theta = 60.4 \pm 1.1^\circ$  ( $t = 10$  min) (Figure 2.3b), the angle of the peptide layer was not affected by the waiting time( $t$ ). Hence, the peptide layer does not rearrange like the DSPH phage in the pH 3.0 solution.

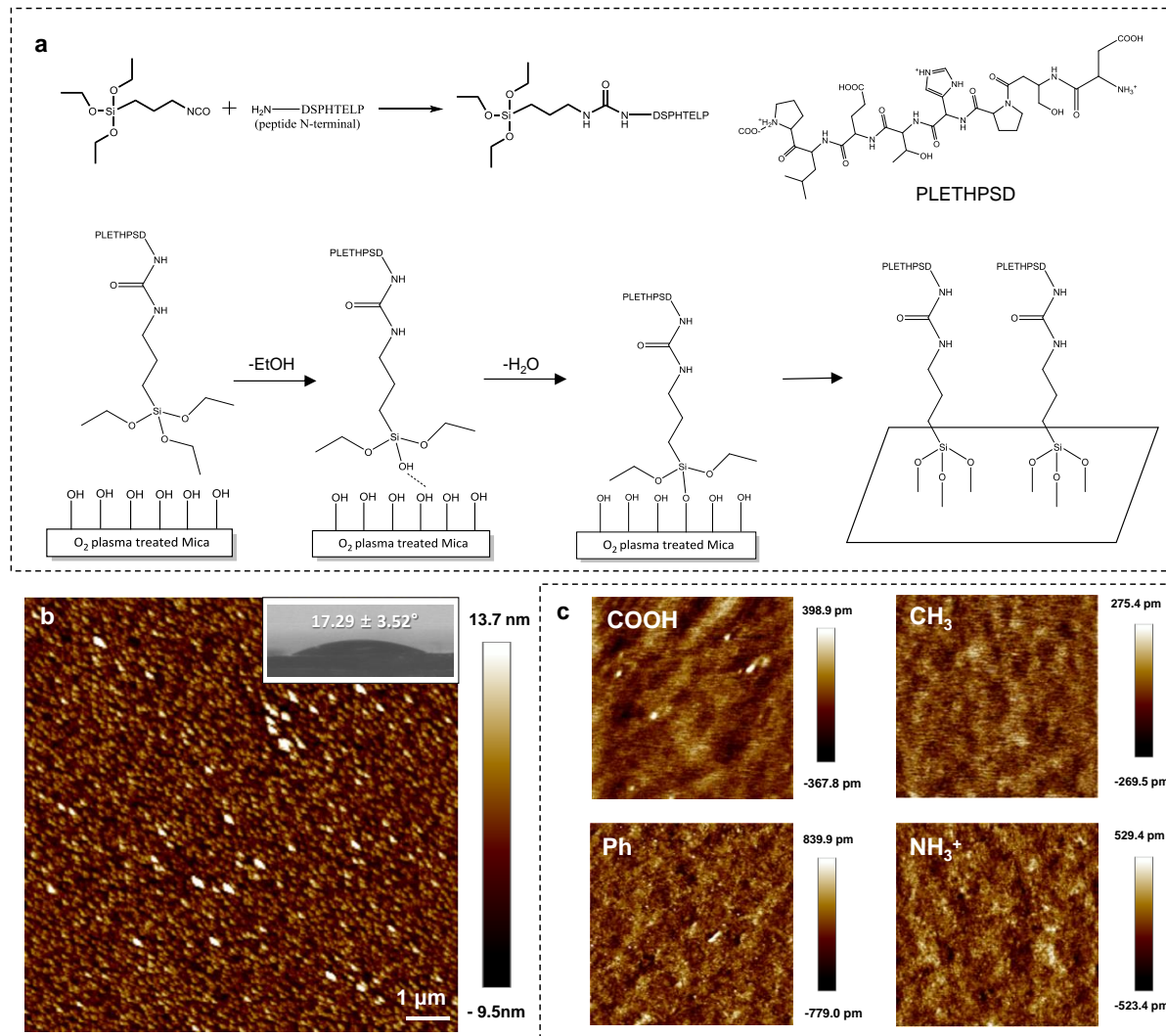


**Figure 3.2.** Surfaces for the SFA measurements. **a** Procedure of preparing the triethoxysilane capped DSPHTELP layer on the O<sub>2</sub> plasma treated mica. **b** AFM image the peptide layer on the mica surface. Inner box is the pH 3.0 KNO<sub>3</sub> solution contact angle image of the peptide. **c**. AFM image of the each functionalized SAMs.

### 3.3.3. Adhesion energy measurements via SFA

Adhesion energies between the DSPHTELP peptide layer and functionalized SAMs were measured and quantified via SFA at pH 3.0 (Figure 3.3) as a function of the contact time ( $t_c$ ). In the case of the COOH-SAM, the adhesion energy is  $W_{ad} = 0.64 \pm 0.23 \text{ mJ m}^{-2}$  at  $t_c = 5 \text{ s}$  to  $W_{ad} = 1.03 \pm 0.59 \text{ mJ m}^{-2}$  at  $t_c = 1 \text{ h}$  (Figure 3.3b). The adhesion force at  $t_c = 5 \text{ s}$ , was stronger than that of the DSPH phage, but it is similar at  $t_c = 1 \text{ h}$  (Figure 2.6b). The peptide sequence forms hydrogen bonding of similar strength to that of the DSPH phage through carboxylic and/or hydroxyl groups from the residue in the aspartate(D), serine(S), threonine(T), and glutamate(E). Moreover, it was identified that the repulsion between the peptide layer and COOH-SAM has a similar tendency to that of the DSPH phage. It is induced by steric repulsion because the COOH-SAM forms dimers by hydrogen bonding with neighboring COOH SAM at the interface and also with water molecules in the  $\text{KNO}_3$  solution<sup>61, 65</sup>.

The adhesion energy with  $\text{CH}_3$ -SAM showed the highest adhesion energy in all functional SAMs ( $W_{ad} = 10.89 \pm 1.44 \text{ mJ m}^{-2}$  at  $t_c = 5 \text{ s}$  to  $W_{ad} = 11.63 \pm 0.42 \text{ mJ m}^{-2}$  at  $t_c = 1 \text{ h}$ ) (Figure 3.3c). The adhesion energy is stronger than that of the DSPH phage. In other words, assuming that the peptide has the same surface density as the DSPH phage, the peptide causes more powerful hydrophobic interactions per unit area than the phage.

However, the adhesion energy between the peptide and Ph-SAM is  $W_{ad} = 4.49 \pm 0.23 \text{ mJ m}^{-2}$  at  $t_c = 5 \text{ s}$  to  $W_{ad} = 4.91 \pm 0.50 \text{ mJ m}^{-2}$  at  $t_c = 1 \text{ h}$ , which is much lower than that of the DSPH phage. Since the dominant adhesion energy types involved with Ph-SAM are  $\pi$ -interactions (e.g.,  $\pi$ - $\pi$  interaction and cation- $\pi$  interaction), the  $\pi$ -interactions appear to be weak. The isoelectric point(pI) value of the DSPHTELP peptide sequence is 4.1, which is lower than that of the DSPH phage (5.3), meaning that the phage has more positively charged amino acids at pH 3.0<sup>42</sup>. Furthermore, the proline that induces the  $\pi$ -interaction located in the c-terminus part of the DSPHTELP sequence. The amino group and carboxylic group of the proline are in the  $-\text{NH}_2^+$  and  $-\text{COO}^-$  forms at pH 3.0, due to their  $\text{pK}_R$  value<sup>58</sup>. As a result, the positively charged amino group of the proline located in the c-terminus interacts with the negatively charged carboxylic group of the neighboring c-terminus proline by electrostatic interaction, reducing  $\pi$ -interactions with  $\text{NH}_3^+$ -SAM and Ph-SAM (Figure 3.d-e)<sup>67, 83, 84</sup>. Therefore, the DSPHTELP peptide sequence has a weaker adhesion energy with the Ph-SAM due to a weaker  $\pi$ -interaction than the DSPH phage.

The difference in adhesion energy strength may be caused by the following differences. The bulk DSPH phage is adsorbed to the mica as a multilayer, and rearrangement occurs when the hydrophilic groups of the amino acids on the phage are exposed over time (Figure 2.3b). However, since the peptide binds covalently to the mica as a monolayer, the steric distance is thinner than that of the phage and the exposed peptides may interact with each other. In addition, the difference in pI value

(Peptide:4.1, DSPH phage:5.3) indicates that other proteins (pIII, pVI, pVIII, and pIX) may influence the adhesion energy with the functional SAMs.

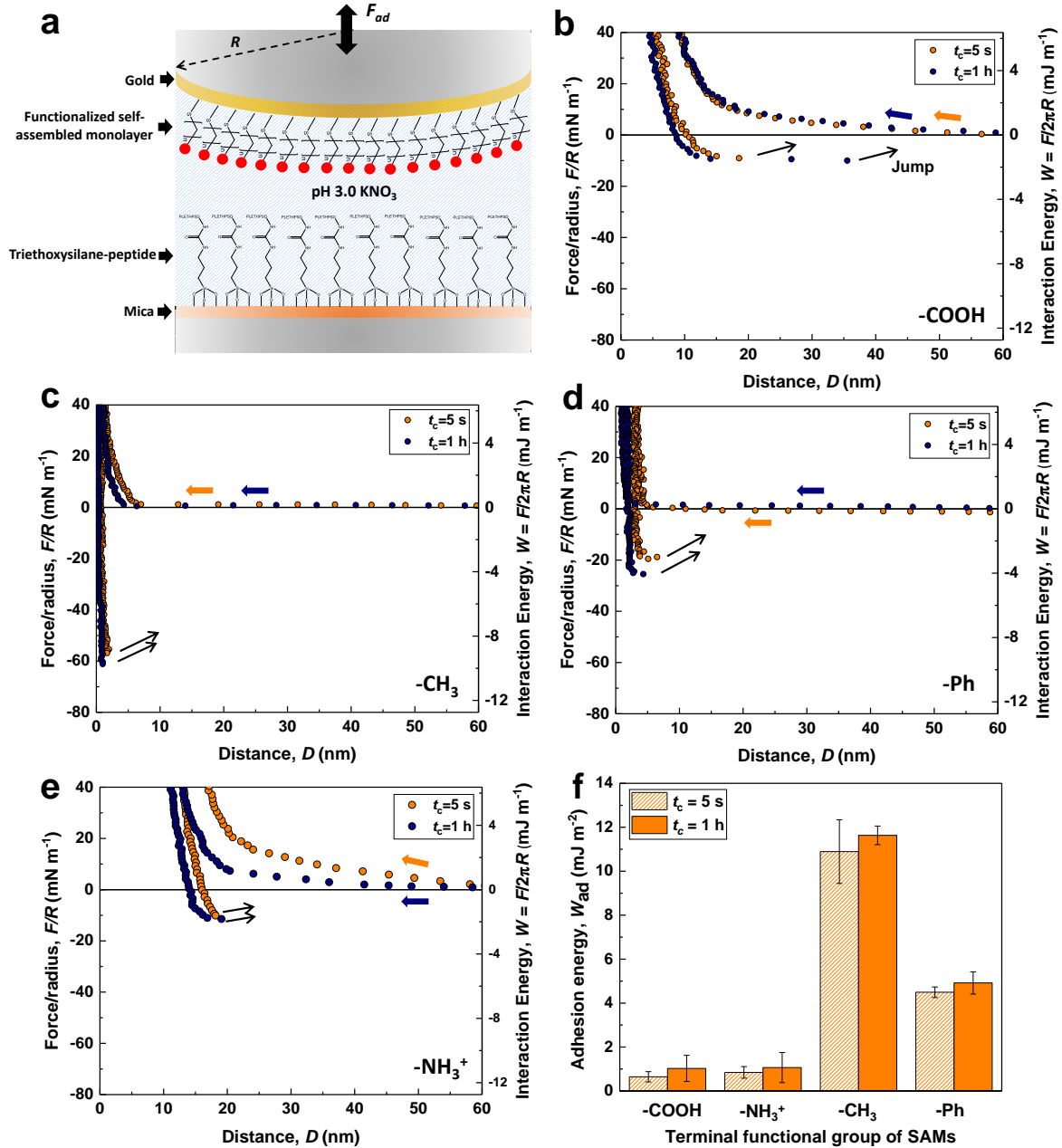


**Figure 3.3.** **a** Experimental Scheme of the SFA measurements. **(a-e)** Force vs. distance profiles measured at pH 3.0. The interactions force of the DSPHTELP layer was measured against functionalized SAMs: **b** -COOH, **c** -CH<sub>3</sub>, **d** -Ph, **e** -NH<sub>3</sub><sup>+</sup>. The orange and navy curves correspond to the force-profiles at contact times ( $t_c$ ) of 5 s and 1 h, respectively. **f** Bar-graph showing the overall adhesion energy ( $W_{ad}$ ) of different SAMs at pH 3.0 as a function of contact time. The error bars represent the s.e.m. where  $n = 3$  in each group.

### 3.4. Discussions

According to the measurement of the adhesion energy of the DSPHTELP peptide, it may be assumed that the binding of SWCNT, which is mainly responsible for hydrophobic and  $\pi$ - $\pi$  interactions, will be strengthened. By measuring the adhesion energy of the synthesized peptides containing only DSPHTELP, I could indirectly deduce the role of the proteins excluding pVIII in the DSPH phage. The adhesion energy may change if the position of amino acid is adjusted in the peptide sequence because interactions between peptides, such as proline dimer formation, may exist. Moreover, it may be necessary to point-mutate the peptide sequence for precise understanding of the role of each amino acid in the sequence. The three-dimensional structure of the peptide should be analyzed by technical tool such as circular dichroism which could analyze secondary structure of peptide and protein.

### 3.5. Conclusions

By focusing on the DSPH phage mentioned in chapter 2 strongly binding to SWCNTs, the DSPHTELP peptide sequence was synthesized, and the adhesion energy with functionalized SAMs was measured and quantified using SFA. As a result, the adhesion energy with  $\text{CH}_3$ -SAM was the strongest, and the hydrophobic interaction was found to be the strongest interaction for the peptide. Hydrogen bonding of the peptide, which was weakest based on the adhesion energy, and the existence of a relatively strong repulsion energy in  $\text{COOH}$ -SAM were identified. It corresponds to the result of the interaction measurements between the DSPH phage and  $\text{COOH}$ -SAM in chapter 2. On the other hand, the adhesion energy with  $\text{Ph}$ -SAM is weaker than that of  $\text{CH}_3$ -SAM, thus, DSPHTELP peptide showed lower adhesion energy via  $\pi$ -interaction compared the DSPH phage. It indicates that peptides excluding the pVIII protein on the DSPH phage have high  $\pi$ -interaction tendencies, and that the proline located in the c-terminus of triethoxysiloxane capped peptide may form dimers by electrostatic interaction to reduce  $\pi$ -interaction. The DSPHTELP peptide sequence, which strongly interacts with hydrophobic and  $\pi$ -interactions, can non-covalently interact with SWCNT like the DSPH phage. Consequently, the peptide can functionalize CNTs with non-covalent interactions in CNT-based biosensors and provide interaction factors, such as amino acid composition, when CNTs detect specific biomolecules. Furthermore, the understanding the biomolecular interactions is expected to contribute design the structure of bio-inspired polymer with the desired functionality.

## Chapter 4. Summary

In this work, the principles and advantages/disadvantages of AFM, QCM-D, and SFA, which are representative technical tools for measuring biopolymer interaction, were investigated. AFM measures the tip-to-surface interaction and is not affected by contamination and fluid behavior due to a small radius tip, but it is not suitable for measuring interactions between deformable soft materials such as biological membranes. QCM-D obtains the mass of adsorbed materials from the frequency change caused by the adsorption of molecules onto the surface of the quartz plate between two metal electrodes. In addition, the viscoelastic properties of the adsorbed materials can be calculated by changes in frequency. However, it is difficult to detect the mass of atoms or small molecules, and it cannot be used on non-uniform and non-smooth surfaces or interfaces. SFA measures the surface-surface adhesion energy directly and obtains the thickness of the material on the substrate at the same time. Nevertheless, as the material is applied to the surface, it is vulnerable to contamination like the adsorption of unwanted particles.

In addition, the characteristics of common non-covalent interactions in biopolymers are identified in chapter 1. The most representative interaction is the van der Waals force, which is a long-distance interaction and caused by an electric dipole moment change in the molecules. The force is influenced by the Hamaker constant, which depends on the properties of the molecules (e.g., dielectric constant, refractive index, and ionization potential). A long-distance force other than the van der Waals force is the electrostatic interaction. It is induced by the charge of the particles and balance of the electric double ionic layer. In aqueous solutions, water molecules surround the surface of the molecule, forming a hydration shell. It occurs more likely on hydrophilic groups or surfaces. While the opposite tendency can be observed on hydrophobic groups or surfaces, which means the water contact angle increases with increasing hydrophobicity. Steric force is generated as the distance between two molecules gets smaller. The exact distance dependence of the force is not known, but the decay is found to be  $1/D^{12}$ . Hydrogen bonding is an interaction between hydrogen atoms that binds covalently to electronegative atoms (F, O, and N). It is stronger than dispersion and dipole-dipole forces, but weaker than covalent and ionic bonding. Furthermore, hydrogen bonding interaction is one of the main interactions that determine the structure of the biopolymer.

In chapter 2, the interaction mechanisms between genetically engineered M13 bacteriophage (DSPH phage) and functional groups (carboxyl, hydroxyl, amine, methyl, and phenyl) were quantified using SFA according to pH conditions. As a result, it was confirmed that the DSPH phage has the highest adhesion energy with the phenyl group by  $\pi$ - $\pi$  and hydrophobic interactions in acidic environment. On the other hand, it showed the lowest adhesion energy with the carboxyl group, indicating that the hydrogen bonding interactions remained relatively weak. Based on the results, DSPH phage-SWCNT complexes were formed at three pH conditions (pH 3.0, 5.0, and 8.0). Hence, the phage interacts



strongly with single walled carbon nanotubes (SWCNTs) through electrostatic, hydrophobic, and  $\pi$ - $\pi$  interactions under acidic condition. Therefore, it suggests that histidine and proline on the DSPH phage induce strong molecular interactions between the phage and SWCNT through  $\pi$ - $\pi$  and hydrophobic interactions. Furthermore, it is experimentally demonstrated that the DSPH-SWCNT complex can be stabilized at high pH through electrostatic and hydration repulsion.

In chapter 3, the adhesion energy of the DSPHTELP peptide sequence, which is the peptide sequence of the pVIII protein in the DSPH phage used in chapter 2, was identified and quantified. The adhesion energy of the peptide is compared to the DSPH phage to analyze the possibility of replacing the phage. Triethoxysilane capped peptide was introduced to bind peptide evenly to the mica substrate, and the adhesion energy was measured with carboxylic, methyl, and phenyl groups at pH 3.0. The hydrogen bonding interaction was weak like the DSPH phage, but hydrophobic interaction is the strongest unlike the DSPH phage, which has  $\pi$ -interaction as its strongest. The adhesion energy caused by  $\pi$ -interaction of the peptide is weaker than the that of the DSPH phage. Hence, it is indirectly confirmed that the proteins on the DSPH phage, other than the pVIII protein, were concerned in the interaction mechanisms of the DSPH phage. The effects of structural differences between the multilayer of the phage on mica and monolayer form of the peptide were also identified. Since CNTs can be combined via hydrophobic and  $\pi$ -interaction, the amino acid composition of the peptide used in this work provide the direction and requirements of the peptide sequence for non-covalently functionalized CNTs.

## Chapter 5. Reference

1. Chautard, E.; Thierry-Mieg, N.; Ricard-Blum, S., Interaction networks: from protein functions to drug discovery. A review. *Pathologie Biologie* **2009**, *57* (4), 324-333.
2. Campbell, S. J.; Gold, N. D.; Jackson, R. M.; Westhead, D. R., Ligand binding: functional site location, similarity and docking. *Current opinion in structural biology* **2003**, *13* (3), 389-395.
3. Gray, J. J., The interaction of proteins with solid surfaces. *Current opinion in structural biology* **2004**, *14* (1), 110-115.
4. Getzoff, E. D.; Geysen, H. M.; Rodda, S. J.; Alexander, H.; Tainer, J. A.; Lerner, R. A., Mechanisms of antibody binding to a protein. *Science* **1987**, *235* (4793), 1191-1196.
5. Ozboyaci, M.; Kokh, D. B.; Corni, S.; Wade, R. C., Modeling and simulation of protein–surface interactions: achievements and challenges. *Quarterly reviews of biophysics* **2016**, *49*.
6. Leckband, D., Measuring the forces that control protein interactions. *Annual review of biophysics and biomolecular structure* **2000**, *29* (1), 1-26.
7. Lifshitz, E. M.; Hamermesh, M., The theory of molecular attractive forces between solids. In *Perspectives in Theoretical Physics*, Elsevier: 1992; pp 329-349.
8. Leckband, D.; Israelachvili, J., Intermolecular forces in biology. *Quarterly reviews of biophysics* **2001**, *34* (2), 105-267.
9. Johansson, P.; Apell, P., Geometry effects on the van der Waals force in atomic force microscopy. *Physical Review B* **1997**, *56* (7), 4159.
10. Zhou, H.-X.; Pang, X., Electrostatic interactions in protein structure, folding, binding, and condensation. *Chemical reviews* **2018**, *118* (4), 1691-1741.
11. Israelachvili, J. N., *Intermolecular and surface forces*. Academic press: 2015.
12. Piel, L., *Ideas of quantum chemistry*. Elsevier: 2006.
13. Desiraju, G. R.; Steiner, T., *The weak hydrogen bond: in structural chemistry and biology*. International Union of Crystal: 2001; Vol. 9.
14. Schuster, P.; Mikenda, W., *Hydrogen bond research*. Springer Science & Business Media: 2012.
15. Woolfson, D. N.; Williams, D. H., The influence of proline residues on  $\alpha$ -helical structure. *FEBS letters* **1990**, *277* (1-2), 185-188.
16. Martinez, C. R.; Iverson, B. L., Rethinking the term “ $\pi$ -stacking”. *Chemical Science* **2012**, *3* (7), 2191-2201.
17. Waters, M. L., Aromatic interactions in model systems. *Current opinion in chemical biology* **2002**, *6* (6), 736-741.
18. Dougherty, D. A., The cation– $\pi$  interaction. *Accounts of chemical research* **2012**, *46* (4),

885-893.

19. Lucas, X.; Bauzá, A.; Frontera, A.; Quinonero, D., A thorough anion– $\pi$  interaction study in biomolecules: on the importance of cooperativity effects. *Chemical science* **2016**, *7* (2), 1038-1050.
20. Makwana, K. M.; Mahalakshmi, R., Implications of aromatic–aromatic interactions: From protein structures to peptide models. *Protein Science* **2015**, *24* (12), 1920-1933.
21. Lee, G. U.; Kidwell, D. A.; Colton, R. J., Sensing discrete streptavidin-biotin interactions with atomic force microscopy. *Langmuir* **1994**, *10* (2), 354-357.
22. Lee, C.-K.; Wang, Y.-M.; Huang, L.-S.; Lin, S., Atomic force microscopy: determination of unbinding force, off rate and energy barrier for protein–ligand interaction. *Micron* **2007**, *38* (5), 446-461.
23. Viani, M. B.; Pietrasanta, L. I.; Thompson, J. B.; Chand, A.; Gebeshuber, I. C.; Kindt, J. H.; Richter, M.; Hansma, H. G.; Hansma, P. K., Probing protein–protein interactions in real time. *Nature Structural & Molecular Biology* **2000**, *7* (8), 644.
24. Geisler, M.; Pirzer, T.; Ackerschott, C.; Lud, S.; Garrido, J.; Scheibel, T.; Hugel, T., Hydrophobic and Hofmeister effects on the adhesion of spider silk proteins onto solid substrates: an AFM-based single-molecule study. *Langmuir* **2008**, *24* (4), 1350-1355.
25. Willemsen, O. H.; Snel, M. M.; Cambi, A.; Greve, J.; De Groot, B. G.; Figdor, C. G., Biomolecular interactions measured by atomic force microscopy. *Biophysical journal* **2000**, *79* (6), 3267-3281.
26. Tagaya, M., In situ QCM-D study of nano-bio interfaces with enhanced biocompatibility. *Polymer Journal* **2015**, *47* (9), 599.
27. Tammelin, T.; Merta, J.; Johansson, L.-S.; Stenius, P., Viscoelastic properties of cationic starch adsorbed on quartz studied by QCM-D. *Langmuir* **2004**, *20* (25), 10900-10909.
28. Dixon, M. C., Quartz crystal microbalance with dissipation monitoring: enabling real-time characterization of biological materials and their interactions. *Journal of biomolecular techniques: JBT* **2008**, *19* (3), 151.
29. Sauerbrey, G., Verwendung von Schwingquarzen zur Wägung dünner Schichten und zur Mikrowägung. *Zeitschrift für physik* **1959**, *155* (2), 206-222.
30. Liu, S. X.; Kim, J.-T., Application of Kelvin–Voigt model in quantifying whey protein adsorption on polyethersulfone using QCM-D. *JALA: Journal of the Association for Laboratory Automation* **2009**, *14* (4), 213-220.
31. Tang, L.; Thevenot, P.; Hu, W., Surface chemistry influences implant biocompatibility. *Current topics in medicinal chemistry* **2008**, *8* (4), 270-280.
32. Andersson, M.; Andersson, J.; Sellborn, A.; Berglin, M.; Nilsson, B.; Elwing, H., Quartz crystal microbalance-with dissipation monitoring (QCM-D) for real time measurements of

blood coagulation density and immune complement activation on artificial surfaces. *Biosensors and Bioelectronics* **2005**, *21* (1), 79-86.

33. Lubarsky, G.; Davidson, M.; Bradley, R., Hydration–dehydration of adsorbed protein films studied by AFM and QCM-D. *Biosensors and Bioelectronics* **2007**, *22* (7), 1275-1281.

34. Huang, R.; Yi, P.; Tang, Y., Probing the interactions of organic molecules, nanomaterials, and microbes with solid surfaces using quartz crystal microbalances: methodology, advantages, and limitations. *Environmental Science: Processes & Impacts* **2017**, *19* (6), 793-811.

35. Dolatshahi-Pirouz, A.; Rechendorff, K.; Hovgaard, M. B.; Foss, M.; Chevallier, J.; Besenbacher, F., Bovine serum albumin adsorption on nano-rough platinum surfaces studied by QCM-D. *Colloids and Surfaces B: Biointerfaces* **2008**, *66* (1), 53-59.

36. Richter, R. P.; Brisson, A. R., Following the formation of supported lipid bilayers on mica: a study combining AFM, QCM-D, and ellipsometry. *Biophysical journal* **2005**, *88* (5), 3422-3433.

37. Ball, V.; Hübsch, E.; Schweiss, R.; Voegel, J.-C.; Schaaf, P.; Knoll, W., Interactions between multivalent ions and exponentially growing multilayers: dissolution and exchange processes. *Langmuir* **2005**, *21* (18), 8526-8531.

38. Israelachvili, J.; Min, Y.; Akbulut, M.; Alig, A.; Carver, G.; Greene, W.; Kristiansen, K.; Meyer, E.; Pesika, N.; Rosenberg, K., Recent advances in the surface forces apparatus (SFA) technique. *Reports on Progress in Physics* **2010**, *73* (3), 036601.

39. Lim, C.; Ko, J.; Jeon, D.; Song, Y.; Park, J.; Ryu, J.; Lee, D. W., Probing molecular mechanisms of M13 bacteriophage adhesion. *Communications Chemistry* **2019**, *2* (1), 1-9.

40. Lee, S. Y.; Lim, J. S.; Harris, M. T., Synthesis and application of virus- based hybrid nanomaterials. *Biotechnology and bioengineering* **2012**, *109* (1), 16-30.

41. Kim, W.-G.; Song, H.; Kim, C.; Moon, J.-S.; Kim, K.; Lee, S.-W.; Oh, J.-W., Biomimetic self-templating optical structures fabricated by genetically engineered M13 bacteriophage. *Biosensors and Bioelectronics* **2016**, *85*, 853-859.

42. Dang, X.; Yi, H.; Ham, M.-H.; Qi, J.; Yun, D. S.; Ladewski, R.; Strano, M. S.; Hammond, P. T.; Belcher, A. M., Virus-templated self-assembled single-walled carbon nanotubes for highly efficient electron collection in photovoltaic devices. *Nature Nanotechnology* **2011**, *6* (6), 377.

43. Yi, H.; Ghosh, D.; Ham, M.-H.; Qi, J.; Barone, P. W.; Strano, M. S.; Belcher, A. M., M13 phage-functionalized single-walled carbon nanotubes as nanoprobes for second near-infrared window fluorescence imaging of targeted tumors. *Nano letters* **2012**, *12* (3), 1176-1183.

44. Chung, W.-J.; Merzlyak, A.; Lee, S.-W., Fabrication of engineered M13 bacteriophages into liquid crystalline films and fibers for directional growth and encapsulation of fibroblasts. *Soft Matter* **2010**, *6* (18), 4454-4459.

45. Lee, J. H.; Warner, C. M.; Jin, H.-E.; Barnes, E.; Poda, A. R.; Perkins, E. J.; Lee,

- S.-W., Production of tunable nanomaterials using hierarchically assembled bacteriophages. *nature protocols* **2017**, *12* (9), 1999.
46. Lee, Y. J.; Yi, H.; Kim, W.-J.; Kang, K.; Yun, D. S.; Strano, M. S.; Ceder, G.; Belcher, A. M., Fabricating genetically engineered high-power lithium-ion batteries using multiple virus genes. *Science* **2009**, *324* (5930), 1051-1055.
47. Nam, Y. S.; Magyar, A. P.; Lee, D.; Kim, J.-W.; Yun, D. S.; Park, H.; Pollom Jr, T. S.; Weitz, D. A.; Belcher, A. M., Biologically templated photocatalytic nanostructures for sustained light-driven water oxidation. *Nature nanotechnology* **2010**, *5* (5), 340.
48. Guo, Q.; Li, F., Self-assembled alkanethiol monolayers on gold surfaces: resolving the complex structure at the interface by STM. *Physical Chemistry Chemical Physics* **2014**, *16* (36), 19074-19090.
49. Adamczyk, Z.; Zaucha, M.; Zembala, M., Zeta potential of mica covered by colloid particles: a streaming potential study. *Langmuir* **2010**, *26* (12), 9368-9377.
50. Lee, D. W.; Lim, C.; Israelachvili, J. N.; Hwang, D. S., Strong adhesion and cohesion of chitosan in aqueous solutions. *Langmuir* **2013**, *29* (46), 14222-14229.
51. Shields, G. C.; Seybold, P. G., *Computational approaches for the prediction of pKa values*. CRC Press: 2013.
52. Zhang, H.; He, H.-X.; Wang, J.; Mu, T.; Liu, Z.-F., Force titration of amino group-terminated self-assembled monolayers using chemical force microscopy. *Applied Physics A* **1998**, *66* (1), S269-S271.
53. Vezenov, D. V.; Noy, A.; Rozsnyai, L. F.; Lieber, C. M., Force titrations and ionization state sensitive imaging of functional groups in aqueous solutions by chemical force microscopy. *Journal of the American Chemical Society* **1997**, *119* (8), 2006-2015.
54. Poggi, M. A.; Lillehei, P. T.; Bottomley, L. A., Chemical force microscopy on single-walled carbon nanotube paper. *Chemistry of Materials* **2005**, *17* (17), 4289-4295.
55. Wang, Q. Self-assembled monolayers as platform for biosensors. Ph.D thesis, Auburn University, 2005.
56. Contreras, A. E.; Steiner, Z.; Miao, J.; Kasher, R.; Li, Q., Studying the role of common membrane surface functionalities on adsorption and cleaning of organic foulants using QCM-D. *Environmental science & technology* **2011**, *45* (15), 6309-6315.
57. Schouteden, K. Self-assembled dithiol monolayers as a surface modifier and tunnel barrier: a scanning probe microscopy study. Master's thesis, Eindhoven University of Technology, Netherlands, 2004.
58. Nelson, D. L.; Lehninger, A. L.; Cox, M. M., *Lehninger principles of biochemistry*. Macmillan: 2008.

59. Liu, D.; Wyttenbach, T.; Bowers, M. T., Hydration of protonated primary amines: effects of intermolecular and intramolecular hydrogen bonds. *International Journal of Mass Spectrometry* **2004**, *236* (1-3), 81-90.
60. Liu, D.; Wyttenbach, T.; Barran, P. E.; Bowers, M. T., Sequential hydration of small protonated peptides. *Journal of the American Chemical Society* **2003**, *125* (28), 8458-8464.
61. Winter, N.; Vieceli, J.; Benjamin, I., Hydrogen-bond structure and dynamics at the interface between water and carboxylic acid-functionalized self-assembled monolayers. *The Journal of Physical Chemistry B* **2008**, *112* (2), 227-231.
62. Zhao, J.; Luo, L.; Yang, X.; Wang, E.; Dong, S., Determination of surface pKa of SAM using an electrochemical titration method. *Electroanalysis: An International Journal Devoted to Fundamental and Practical Aspects of Electroanalysis* **1999**, *11* (15), 1108-1113.
63. Rupley, J. A.; Careri, G., Protein hydration and function. In *Advances in protein chemistry*, Elsevier: 1991; Vol. 41, pp 37-172.
64. Bone, S.; Pethig, R., Dielectric studies of protein hydration and hydration-induced flexibility. *Journal of molecular biology* **1985**, *181* (2), 323-326.
65. Yang, A.-C.; Weng, C.-I., Influence of alkanethiol self-assembled monolayers with various tail groups on structural and dynamic properties of water films. *The Journal of chemical physics* **2008**, *129* (15), 154710.
66. Hu, J.; Barbour, L. J.; Gokel, G. W., The indole side chain of tryptophan as a versatile  $\pi$ -donor. *Journal of the American Chemical Society* **2002**, *124* (37), 10940-10941.
67. Zondlo, N. J., Aromatic-proline interactions: Electronically tunable CH/ $\pi$  interactions. *Accounts of chemical research* **2012**, *46* (4), 1039-1049.
68. Liao, S.-M.; Du, Q.-S.; Meng, J.-Z.; Pang, Z.-W.; Huang, R.-B., The multiple roles of histidine in protein interactions. *Chemistry Central Journal* **2013**, *7* (1), 44.
69. Yamada, S., Cation- $\pi$  interactions in organic synthesis. *Chemical reviews* **2018**, *118* (23), 11353-11432.
70. Lim, C.; Lee, D. W.; Israelachvili, J. N.; Jho, Y.; Hwang, D. S., Contact time-and pH-dependent adhesion and cohesion of low molecular weight chitosan coated surfaces. *Carbohydrate polymers* **2015**, *117*, 887-894.
71. Flynn, C. E.; Lee, S.-W.; Peelle, B. R.; Belcher, A. M., Viruses as vehicles for growth, organization and assembly of materials. *Acta Materialia* **2003**, *51* (19), 5867-5880.
72. Levine, Z. A.; Rapp, M. V.; Wei, W.; Mullen, R. G.; Wu, C.; Zerze, G. H.; Mittal, J.; Waite, J. H.; Israelachvili, J. N.; Shea, J.-E., Surface force measurements and simulations of mussel-derived peptide adhesives on wet organic surfaces. *Proceedings of the National Academy of Sciences* **2016**, *113* (16), 4332-4337.

73. Qiu, W. Q.; Folstein, M. F., Insulin, insulin-degrading enzyme and amyloid- $\beta$  peptide in Alzheimer's disease: review and hypothesis. *Neurobiology of aging* **2006**, *27* (2), 190-198.
74. Cicero, A. F.; Fogacci, F.; Colletti, A., Potential role of bioactive peptides in prevention and treatment of chronic diseases: a narrative review. *British journal of pharmacology* **2017**, *174* (11), 1378-1394.
75. Torchilin, V. P.; Lukyanov, A. N., Peptide and protein drug delivery to and into tumors: challenges and solutions. *Drug discovery today* **2003**, *8* (6), 259-266.
76. Levy-Nissenbaum, E.; Radovic-Moreno, A. F.; Wang, A. Z.; Langer, R.; Farokhzad, O. C., Nanotechnology and aptamers: applications in drug delivery. *Trends in biotechnology* **2008**, *26* (8), 442-449.
77. Ideker, T.; Sharan, R., Protein networks in disease. *Genome research* **2008**, *18* (4), 644-652.
78. Strehlitz, B.; Nikolaus, N.; Stoltenburg, R., Protein detection with aptamer biosensors. *Sensors* **2008**, *8* (7), 4296-4307.
79. Leca Bouvier, B.; Blum, L. J., Biosensors for protein detection: a review. *Analytical Letters* **2005**, *38* (10), 1491-1517.
80. Vigneshvar, S.; Sudhakumari, C.; Senthilkumaran, B.; Prakash, H., Recent advances in biosensor technology for potential applications—an overview. *Frontiers in bioengineering and biotechnology* **2016**, *4*, 11.
81. Wang, J., Carbon- nanotube based electrochemical biosensors: A review. *Electroanalysis: An International Journal Devoted to Fundamental and Practical Aspects of Electroanalysis* **2005**, *17* (1), 7-14.
82. Maehashi, K.; Matsumoto, K., Label-free electrical detection using carbon nanotube-based biosensors. *Sensors* **2009**, *9* (7), 5368-5378.
83. Busch, S.; Lorenz, C. D.; Taylor, J.; Pardo, L. C.; McLain, S. E., Short-range interactions of concentrated proline in aqueous solution. *The Journal of Physical Chemistry B* **2014**, *118* (49), 14267-14277.
84. Biedermannova, L.; Riley, K. E.; Berka, K.; Hobza, P.; Vondrasek, J., Another role of proline: stabilization interactions in proteins and protein complexes concerning proline and tryptophane. *Physical Chemistry Chemical Physics* **2008**, *10* (42), 6350-6359.

## Chapter 6. Acknowledgement

3 년 반 동안 실험실에서 함께 한 IPCL 구성원들 감사합니다. 학부생 인턴부터 석사과정 2 년까지 많은 고민 상담과 연구 지식을 가르쳐주신 이동욱 교수님께 정말 감사드립니다. 또한 SFA 기기 작동법들을 하나하나 알려주시고, 논문 개재까지 많은 조언을 해주신 임찬웅 박사님 감사합니다. 실험 함께 열심히 한 진우, 유정이, 항상 랩장으로서 고생하고 잘 챙겨주는 진태 오빠, 실험에서 많은 도움을 준 광연 오빠, 실험실에서만 아니라 일상에서 늘 같이 하며 힘이 되어 준 지은이 모두 감사합니다. 덕분에 IPCL 에서 정말 좋은 기억들을 많이 남기고 갈 수 있었습니다.

바쁘신 와중에 학위논문심사 위원으로서 졸업논문과 학위 디펜스에 많은 조언을 해주신 류정기 교수님, 김소연 교수님 감사드립니다. 논문 영어 교정을 열심히 해준 현우, 같이 졸업하면서 졸업 준비 과정에서 도움을 준 주학 오빠 감사합니다.

UNIST 라는 곳에서 처음으로 선배가 되어준 지은 언니, 혁중 오빠, 재훈 오빠 정말 고맙습니다. 취업 준비 하면서 조언과 도움을 많이 준 윤선이, 수인이, 박수희 멘토님 감사합니다. 마지막으로 항상 곁에서 응원해주시는 부모님! 늘 감사드립니다.